UNIVERSITÀ DEGLI STUDI DI PADOVA

Dipartimento di Fisica e Astronomia "Galileo Galilei"

Master Degree in Astrophysics and Cosmology

Final dissertation

Abundance and dynamical properties of the ultradense dark matter halos

Thesis supervisor
Prof. Sabino Matarrese

Candidate
Diana Kulubayeva

Academic Year 2022/23

Abstract

The extreme density fluctuations necessary to produce primordial black holes (PBHs) also lead to the formation of a much greater abundance of dark matter ultradense halos that form during the radiation epoch. The aim of this thesis is to explore in detail the dynamics, properties and statistical abundance of these dark matter mini- halos from its earliest formation, during the radiation epoch, up to the late-time Universe.

Dedication

To my dad.

Declaration

I declare that this thesis was composed by myself, that the work contained herein is my own except where explicitly stated otherwise in the text, and that this work has not been submitted for any other degree or processional qualification except as specified.

Acknowledgements

I would like to express my sincere gratitude and appreciation to all those who have contributed to the completion of this master's thesis. First and foremost, I extend my deepest thanks to my thesis supervisor, Prof. Matarrese, for his invaluable guidance, unwavering support, and insightful feedback throughout the entire research process. I am also grateful to my dad for his constant love, encouragement, and belief in my abilities. His support has been a source of motivation throughout my academic pursuits. Last but not least, I want to extend my gratitude to the Physics and Astronomy Department at the University of Padua for their lectures and resources that allowed me to build a strong foundation to conduct further research in cosmology.

Contents

Chapter 1

Introduction

1.1 History of the Universe

The history of the Universe starts with the Big Bang (BB), when the whole Universe was concentrated and compressed in an extremely dense state, called initial singularity. Eventually leading to a massive explosion otherwise known as an accelerated expansion of the Universe, called inflation. During inflation, initial energy density fluctuations were smoothed out and acted as seeds to the structures of the Universe. This took place approximately from 10^{-36} to 10^{-32} seconds after the Big Bang. After which the radiation dominated epoch took place, when the Universe became dominated by relativistic particles.

As the time progressed the Universe kept expanding and the cosmic plasma was cooling down, allowing the production of light elements. This process is called Big Bang Nucleosynthesis (BBN) and it took place after 3 to 20 minutes from the BB. During this phase, the Universe was cool enough for protons and neutrons to combine to form the nuclei of light elements like hydrogen, helium, and trace amounts of lithium.

Approximately after 50 to 70 thousands years after BB, the matter-radiation equality epoch took place, leading to the matter domination of the Universe. The energy density fluctuations at that point grow via gravitational attraction of the surrounding matter to the denser regions. These regions are the seeds for the large structures of the Universe that we see today.

The cosmic plasma was still hot enough to keep photons in thermal equilibrium until around 380 000 years after the Big Bang, hence the Universe before that time was opaque to the observer. Afterwards, there is the moment of the last scattering of photons and the very first light that we are able to see today, called cosmic microwave background radiation (CMB).

1.2 Primordial Fluctuations

Inflation provides a mechanism for generating the primordial perturbations, although the details are still unknown, there is no certain theory of inflation. Primordial fluctuations obey (quasi-)Gaussian statistics and hence can be described by the power spectrum. The precise measurements of the primordial power spectrum is performed with the help of CMB temperature anisotropies and polarization as well as through large-scale structure probes.

There are scalar, vector and tensor perturbations, but scalar perturbations are of specific interest for us, since they give rise to the variations of energy density. Scalar

perturbations provide indeed the dominant contribution to the anisotropies observed in the CMB and are responsible for the large-scale distribution of galaxies.

The seed for dark matter fluctuations was laid down during the inflationary epoch, a phase of rapid exponential expansion in the early Universe. Quantum fluctuations during inflation led to variations in the density of all matter, including dark matter. The fluctuations in dark matter density were initially small, but over time, regions with slightly higher densities experienced stronger gravitational attraction, causing them to pull in more matter. This gravitational instability led to the growth of structures from small density fluctuations. Dark matter fluctuations drove a process called hierarchical clustering, where small dark matter halos merged to form larger ones. These halos formed very early and are extremely dense, they acted as gravitational attractors, pulling in additional dark matter and influencing the distribution of both dark and visible matter. The growth of dark matter fluctuations set the stage for the formation of the cosmic web – a complex network of filaments, voids, and galaxy clusters. These structures represent the large-scale distribution of dark matter in the Universe. The regions of higher dark matter density, called halos, are where galaxies and galaxy clusters form. The size and properties of these halos depend on the initial fluctuations in dark matter density.

1.3 Probes via Ultradense Dark Matter Halos

Although the nature of dark matter halos make them invisible, they still have some observational features. Ultradense minihalos that formed in the radiation epoch, being extremely, dense affect the paths of light from distant objects such as stars, causing gravitational lensing. This effect provides a way to indirectly map the distribution of dark matter in the Universe.

Another way to detect dark matter and explain its origin is the matter-antimatter production and annihilation, the equilibrium of pair production was disturbed as a result of the Universe's expansion and cooling down, leaving a relic behind in terms of dark matter. This scenario assumes that dark matter annihilation could produce detectable radiation in the cores of ultradense minihalos.

This master thesis starts with the primordial perturbations in dark matter that lead to the formation of dark matter halos in Chapter 2. Chapter 3 covers the dynamics of collapsing overdense region in the radiation dominated epoch for spherical collapse model (Sec.3.1, 3.2) and ellipsoidal collapse (Sec.3.3). Although the collapse takes place at RD stage, the actual formation of an ultradense minihalo happens only at local matter domination. Chapter 4 starts with a simple spherical collapse model in matter domination epoch (Sec.4.1). The next section of this chapter covers subsequent accretion onto ultradense minihalo that formed at the radiation dominated epoch (Sec.4.2). Chapter 5 explores properties of dark matter halos, such as final radius of the core (Sec.5.1), density profiles and structure of the ultradense dark matter halos (Sec.5.2-5.6). Chapter 6 talks about the Press-Schechter formalism (Sec.6.1), its refined version, excursion set formalism (Sec.6.2) and summarizes statistical abundance of dark matter halos and primordial black holes (Sec.6.3, 6.4). Chapter 7 starts with an introduction to gravitational microlensing in the scope of ultradense dark matter halos (Sec.7.1). Explores the detectability of microlensing events (Sec.7.2) and possibilities of identifying meaningful constraints on primordial black holes (Sec.7.3). The last section of this chapter provides the routine to calculate the constraints on primordial power spectrum amplitude (Sec.7.4).

Chapter 2

Primordial Fluctuations

2.1 Introduction

Primordial perturbations are the initial irregularities in the density distribution of matter in the early Universe. These fluctuations arise during cosmic inflation and are imprinted on the Universe's fabric. They serve as the "seeds" for the growth of cosmic structures. Regions with slightly higher densities have a stronger gravitational pull, causing them to attract more matter over time. This leads to an amplification of density fluctuations, resulting in the growth of structures. As density fluctuations grow, regions become increasingly overdense compared to their surroundings. The overdense regions collapse under their self-gravity, forming dark matter halos. These halos act as gravitational attractors, pulling in additional matter from their surroundings and serving as the building blocks for larger structures. Smaller dark matter halos merge over time to form larger and more massive halos. This hierarchical growth continues as halos merge and accrete matter, ultimately leading to the formation of massive galaxy clusters and superclusters. In this chapter, we will see what kind of primordial perturbations give rise to dark matter overdensities and eventual dark matter halo formation.

Primordial perturbations can be classified into three main types: scalar, vector, and tensor perturbations. These classifications are based on the way the perturbations affect different properties of the cosmic fluid, such as density, velocity, and gravitational waves. Scalar perturbations are fluctuations in the density of matter and energy in the Universe. These perturbations lead to variations in the curvature of spacetime and affect the distribution of matter. Scalar perturbations are responsible for the formation of structures like galaxies, galaxy clusters, and the anisotropies observed in the cosmic microwave background radiation. Vector perturbations involve fluctuations in the velocity field of the cosmic fluid. These perturbations describe the possible deviations from uniform motion along a particular direction. Unlike scalar perturbations, vector perturbations do not play a significant role in structure formation on large scales, and their effects are usually subdominant compared to scalar perturbations. Tensor perturbations are associated with gravitational waves, which are ripples in the fabric of spacetime itself. These perturbations do not directly affect matter density or velocity but are rather a consequence of the Einstein field equations of general relativity. Tensor perturbations can be detected through their influence on the polarization patterns in the cosmic microwave background radiation. Scalar perturbations are the most significant and relevant type when it comes to structure formation and cosmological observations. They are responsible for the majority of the features we observe in the large-scale structure of the Universe and the cosmic microwave background. Vector and tensor perturbations, while important in their own right, typically have smaller effects and are of primary interest in specialized scenarios

and analyses.

This Chapter is focused on the scalar perturbations in the dark matter energy density. First, in the Section 2.2, I will examine the different modes of scalar perturbations, namely, adiabatic and isocurveture modes. Adiabatic and isocurvature modes are two different types of scalar perturbations that can exist in the early Universe. These modes refer to the initial conditions of density fluctuations in various components of the cosmic fluid, including both dark matter and baryonic matter. They have distinct effects on the large-scale structure formation and the cosmic microwave background radiation. Section 2.3 introduces the tool, which helps to characterize the primordial perturbations, namely, primordial power spectrum. This Section provides mathematical machinery to be able to calculate the primordial power spectrum and its amplitude. Section 2.4 introduces the evolution of overdensity in the radiation dominated epoch. This paramter is of a great importance, since it will help to understand the eventual dynamics of the overdense region. Section 2.5 focuses and derives the dark matter perturbations, particularly the cold dark matter. Throughout this thesis, it is assumed that the dark matter is cold enough to form clumps and structures. Finally, Section 2.6 examines the density perturbations that can lead to primordial black hole formation. Primordial black holes require much higher overdensities for their formation compared to dark matter halos, the connection between these phenomena is that they originate from the same power spectrum, so Primordial Black Holes can provide potentially useful insights into the topic of dark matter halos formation.

2.2 Scalar Perturbations in Adiabatic and Isocurvature Modes

Initial data for scalar perturbations is defined deep at radiation domination epoch. At that time the modes of interest are superhorizon modes. Perturbation remain superhorizon at temperature of 1 MeV, so we can always treat dark matter and baryons as non-relativistic and neutrino and dark matter as decoupled. When studying superhorizon perturbations we often consider formal limit, which is $\eta \longrightarrow 0$. Possible initial data and hence types of perturbations are conveniently decomposed into linear independent parts adiabatic and isocurvature modes.

The adiabatic mode corresponds to the situation where relativistic matter, which is the dominant component at the early epoch, has non-vanishing energy density perturbations, [21]. These perturbations affect all components of the Universe, including dark matter, baryons, radiation, and dark energy, in the same way. Adiabatic perturbations lead to variations in the gravitational potential across different regions of the Universe. As regions with higher potential wells attract more matter, dark matter halos start forming in these regions of enhanced density. Adiabatic perturbations are considered to be the primary source of density fluctuations that lead to the formation of large-scale cosmic structures, including galaxies, galaxy clusters, and dark matter halos.

The main property of baryon and cold dark matter (CDM) isocurvature modes is that there is no perturbation of the relativistic component deep at radiation domination, but the composition of the medium is spatially inhomogeneous, [21]. Isocurvature perturbations refer to fluctuations that alter the relative densities of different components of the Universe, such as dark matter and baryons, while keeping the total energy density constant. Isocurvature perturbations do not create variations in the gravitational potential in the same way adiabatic perturbations do. As a result, isocurvature perturbations can affect the way dark matter halos form and evolve. Isocurvature perturbations might

lead to differences in the growth of dark matter halos in regions with varying densities of dark matter and baryons. Depending on the specific nature of isocurvature fluctuations, this could impact the abundance and properties of halos differently than adiabatic fluctuations.

2.3 Power Spectrum for Scalar Perturbations

The power spectrum is a key quantity used to characterize cosmological perturbations. It describes the statistical distribution of the amplitude of perturbations as a function of scale or wavenumber. We focus on the scalar perturbations. Their properties are well known from the observations. They are adiabatic, without decaying mode and the admixture of isocurvature modes is constrained.

From the observations we know that the primordial field that specifies the initial data for the adiabatic mode is the Gaussian Random Field, $\mathcal{R}(\mathbf{x})$. This field is determined by the two-point correlation function, [21]

$$< \mathcal{R}(\mathbf{k})\mathcal{R}(\mathbf{k'}) >= \frac{P_{\mathcal{R}}(k)}{(2\pi)^3}\delta(\mathbf{k}+\mathbf{k'}) \tag{2.1}$$

where $P_{\mathcal{R}}(k)$ is the scalar function, the power spectrum.

It is convenient to introduce the following quantity, which is power spectrum

$$\mathcal{P}_{\mathcal{R}}(k) = \frac{k^3}{2\pi^2}P_{\mathcal{R}}(k) \tag{2.2}$$

From (2.1), we can see that the fluctuation of the random field, $\mathcal{R}(\mathbf{x})$ is

$$< \mathcal{R}^2(\mathbf{x}) >= \int_0^\infty \frac{dk}{k}\mathcal{P}_{\mathcal{R}}(k) \tag{2.3}$$

where $\mathcal{P}_{\mathcal{R}}(k)$ is the contribution to the fluctuation coming from a decimal interval of momenta around k. This contribution can be constant, independent of k for the flat spectrum or Harrison-Zeldovich spectrum, [22], [37].

The procedure to obtain the expression (2.3) is the following:

$$< \phi^2(\mathbf{x}) >= \int d^3k d^3k' e^{i(\mathbf{k}+\mathbf{k'})\mathbf{x}} < \phi(\mathbf{k})\phi(\mathbf{k'}) >= \int d^3k \frac{P(\mathbf{k})}{(2\pi)^3} \tag{2.4}$$

Now, integrate the angular part,

$$< \phi^2(\mathbf{x}) >= \int_0^\infty 4\pi dk \frac{k^2}{(2\pi)^3}\frac{2\pi^2}{k^3}\mathcal{P}_{\mathcal{R}}(k) = \int_0^\infty \frac{dk}{k}\mathcal{P}_{\mathcal{R}}(k) \tag{2.5}$$

where $\phi(\mathbf{x})$ is the Gaussian random field.

Sometimes another notation is used,

$$\Delta^2_{\mathcal{R}}(k) \equiv \mathcal{P}_{\mathcal{R}}(k) \tag{2.6}$$

where $\Delta_{\mathcal{R}}(k)$ is the amplitude of the scalar perturbations of momentum k.

From the observations we know that the spectrum of the scalar perturbations is nearly flat. From this we can naturally parameterize the spectrum as the power-law, which looks as follows:

$$\mathcal{P}_{\mathcal{R}}(k) = \mathcal{A}_{\mathcal{R}}\left(\frac{k}{k_*}\right)^{n_s-1} \tag{2.7}$$

Here k_* is some conveniently chosen fiducial momentum and $\mathcal{A}_\mathcal{R}$ is nothing else, but the power spectrum at k_*, $\mathcal{A}_\mathcal{R} = \mathcal{P}_\mathcal{R}(k_*)$, $(n_s - 1)$ is the spectral tilt.

In general, the power spectrum doesn't have to have the power-law behavior. In order to account for the other possibility, we introduce another parameter, which is called running index:

$$\frac{dn_s}{d\log k} \equiv \frac{dn_s}{d\log k}(k_*) \tag{2.8}$$

Then the power spectrum becomes, [21]

$$\mathcal{P}_\mathcal{R}(k) = \mathcal{A}_\mathcal{R}\left(\frac{k}{k_*}\right)^{n_s - 1 + \frac{dn_s}{d\log k}\log\frac{k}{k_*}} \tag{2.9}$$

The running index is the rate of the spectral index variation near $k = k_*$.

Assuming that there are no tensor perturbations and no momentum dependence of the tilt, we can obtain the following values by fitting the set of cosmological data, [26].

$$\mathcal{A}_\mathcal{R} = (2.36 \pm 0.09) \times 10^{-9}, \qquad n_s = 0.960 \pm 0.014 \tag{2.10}$$

for $k_*/a_0 = 0.002 Mpc^{-1}$. Hence, the primordial scalar amplitude is

$$\Delta_\mathcal{R} \simeq 5 \times 10^{-5} \tag{2.11}$$

2.4 Evolution of Perturbations at Radiation Domination Epoch

Evolution of radiation density perturbation at the radiation dominated epoch obeys the following law [35]:

$$\delta_r = x f(x) + \frac{3x^2}{x^2 + 6}\frac{d}{dx} f(x) \tag{2.12}$$

The growing mode of this equation is

$$f(x) = A_{in} j_1(\frac{x}{\sqrt{3}}) \tag{2.13}$$

where j_1 is the spherical Bessel function, A_{in} is normalization constant, $x = k\eta$, k is comoving perturbation wave vector.

The physical perturbation wavelength and the mass within this region:

$$\lambda_{ph}(\eta) = a(\eta)\frac{2\pi}{k} \qquad M_x = \frac{4\pi}{3}\rho_0\left(\frac{\lambda_{ph}(t_0)}{2}\right)^3 \tag{2.14}$$

Adiabatic perturbations in nonrelativistic matter with $x \ll 1$ obey $\delta = 3\delta_r/4$. Whereas the analytic solution in the limits $x \ll 1$ and $x \gg 1$ is, [18]

$$\delta = \frac{3A_{in}}{2}\left[\ln\left(\frac{x}{\sqrt{3}}\right) + \gamma_E - \frac{1}{2}\right] \tag{2.15}$$

which can be used to the linear order in the limit $\delta \ll 1$.

2.5 Dark Matter Perturbations

We start by considering adiabatic mode at the radiation domination epoch (RD). The dark matter perturbations will be sourced by the following potential, [21]:

$$\Phi(\eta) = \Phi_{(i)} 3\sqrt{\frac{\pi}{2}} \frac{1}{(u_s k\eta)^{3/2}} J_{3/2}(u_s k\eta) = \tag{2.16}$$

$$= -3\Phi_{(i)} \frac{1}{(u_s k\eta)^2} \left(\cos(u_s k\eta) - \frac{\sin(u_s k\eta)}{u_s k\eta} \right) \tag{2.17}$$

In general, the perturbations defined as

$$\delta \equiv \frac{\delta\rho}{\rho} \tag{2.18}$$

obey the following equations, [21]:

$$\delta'_\lambda + 3\frac{a'}{a}(u^2_{s,\lambda} - w_\lambda)\delta_\lambda - (1+w_\lambda)k^2 v_\lambda = 3(1+w_\lambda)\Phi' \tag{2.19}$$

$$\big((1+w_\lambda)v_\lambda\big)' + \frac{a'}{a}(1-3w_\lambda)(1+w_\lambda)v_\lambda + u^2_{s,\lambda}\delta_\lambda = -(1+w_\lambda)\Phi \tag{2.20}$$

We set $w = u_s^2 = 0$, and they become:

$$\delta'_{CDM} - k^2 v_{CDM} = 3\Phi' \tag{2.21}$$

$$v'_{CDM} + \frac{1}{\eta} v_{CDM} = -\Phi \tag{2.22}$$

In the last equation we used the approximation $a \propto \eta$ at RD. Here $u_s^2 = \frac{\delta p}{\delta \rho}$ and $w = \frac{p}{\rho}$ and they are not the same.

The potential (2.16) decrease rapidly during late times, so $u_s k\eta \ll 1$, then the equations (2.21), (2.22) become homogeneous:

$$\delta'_{CDM} - k^2 v_{CDM} = 0 \tag{2.23}$$

$$v'_{CDM} + \frac{1}{\eta} v_{CDM} = 0 \tag{2.24}$$

The solution to (2.24) is

$$v_{CDM} = \frac{c_1}{k^2 \eta} \tag{2.25}$$

where c_1 is a dimensionless constant.

Then the solution to (2.23) is

$$\delta_{CDM} = c_1 \log k\eta + c_2 \tag{2.26}$$

So, we can see that the CDM perturbations grow logarithmically at the RD epoch.

However, if there were no sources on the right hand side of equations 2.21, 2.22, then the logarithmically growing part would be absent, since it would diverge as $\eta \to 0$, meaning that it would be the decaying mode or primordial perturbations and we know that the decaying mode vanish.

To find the constants, we first solve the equation (2.22) with the potential (2.16). The solution is

$$v_{CDM} = -\frac{1}{\eta}\int_0^\eta d\tilde{\eta}\tilde{\eta}\Phi(\tilde{\eta}) \tag{2.27}$$

so that $v_{CDM} \to 0$ as $\eta \to 0$. And then the solution to (2.21) becomes:

$$\delta_{CDM}(\eta) = 3\Phi(\eta) + c - k^2\int_0^\eta \frac{d\hat{\eta}}{\hat{\eta}}\int_0^{\hat{\eta}} d\bar{\eta}\bar{\eta}\Phi(\bar{\eta})\log\frac{\eta}{\tilde{\eta}} \tag{2.28}$$

The potential decreases as $u_s k\eta \gg 1$, the integral converges and the solution becomes:

$$\delta_{CDM}(\eta) = \delta_{CDM,(i)} - 9\Phi_{(i)} \times \left(\log(u_s k\eta) + \mathbf{C} - \frac{2}{3}\right) \tag{2.29}$$

where $\mathbf{C} = 0.577$ is the Euler constant. In order to obtain these results, we used $u_s^2 = 1/3$ and the following integrals:

$$\sqrt{\frac{\pi}{2}}\int_0^\infty J_{3/2}(z)\frac{dz}{\sqrt{z}} = 1, \qquad \sqrt{\frac{\pi}{2}}\int_0^\infty J_{3/2}(z)\log z\frac{dz}{\sqrt{z}} = 1 - \mathbf{C} \tag{2.30}$$

From the solution 2.29, we can see that at large values of $u_s k\eta$ the dominant term will be the logarithmic one and the initial value, $\delta_{CDM,(i)}$ becomes not important.

Using the fact that the gravitational potential obeys

$$\Phi = -\frac{2}{3}\zeta = -\frac{2}{3}\mathcal{R} \tag{2.31}$$

and recalling that at the RD stage we have

$$\delta_{CDM} = \delta_B = \delta_M = \frac{3}{4}\delta_{rad} = \frac{3}{4}\delta_\gamma = -\frac{3}{2}\Phi = \mathcal{R} \tag{2.32}$$

we get the perturbation of dark matter for the subhorizon adiabatic mode, [21]:

$$\delta_{CDM} = -9\Phi_{(i)}\left(\log\frac{k\eta}{\sqrt{3}} + \mathbf{C} - \frac{1}{2}\right) \tag{2.33}$$

2.6 Formation of Primordial Black Holes

Primordial black holes and dark matter halos originate from common spectrum, [18]. Consider a region with the density $\rho > \rho_c = 3H^2/8\pi G$. The evolution of this region can be investigated independently of the background evolution. This region can collapse to form a primordial black hole (PBH), if the relative radiation density fluctuation $\delta_H = \frac{\rho-\rho_c}{\rho_c}$ will be in the range:

$$\delta_c \le \delta_h \le 1 \tag{2.34}$$

where $\delta_c = 1/3$, which corresponds to the condition that the radius of the region stops/ exceeds the Jeans radius, $\frac{ct}{\sqrt{3}}$. The other inequality corresponds to the formation of a PBH. The mass of a forming PBH:

$$M_{BH} = \frac{M_H}{3^{3/2}} \tag{2.35}$$

where M_H is the mass within the horizon.

The mass of a PBH as a result of a critical gravitational collapse is:

$$M_{BH} = AM_H(\delta_H - \delta_c)^\gamma \tag{2.36}$$

We will consider a broader range for δ_c:

$$1/2 \leq \delta_c \leq 0.7 \tag{2.37}$$

It is assumed that there is s sharp peak in the perturbation spectrum at the scale $\xi = \frac{r}{a(t)}$. The threshold for a PBH is too large to result in a PBH formation for every ξ scale fluctuation. The fluctuations are preserved till the matter domination epoch.

The expressions for the mass within the horizon, M_H and the mass of the dust component in the fluctuations at the same comoving scale are:

$$M_H = \frac{4\pi}{3}\rho_H(a(\eta_H)\xi)^3 \qquad\qquad M_x = \frac{4\pi}{3}\rho_0(a(\eta_0)\xi)^3 \tag{2.38}$$

At the horizon scale $a(\eta_H)\xi = 2ct_H$ and the densities are:

$$\rho_H = \frac{3}{32\pi G t_H^2} \qquad\qquad \rho_0 = \rho_{eq}\left(\frac{a_{eq}}{a_0}\right)^3 \tag{2.39}$$

Now we can express M_H in terms of M_x:

$$M_H = \frac{1}{2^{2/3}}\left(\frac{3}{2\pi}\right)^{1/6}\frac{M_x^{2/3}c}{G^{1/2}\rho_{eq}^{1/6}} \tag{2.40}$$

$$t_H = \frac{GM_H}{c^3} \tag{2.41}$$

We define the rms fluctuation δ_H as:

$$\Delta_H \equiv < \delta_H^2 >^{1/2} \tag{2.42}$$

The fraction of PBH formation at time t_H is

$$\beta = \int_{\delta_c}^{1}\frac{d\delta_H}{\sqrt{2\pi}\Delta_H}e^{-\frac{\delta_H^2}{2\Delta_H^2}} \simeq \frac{\Delta_H}{\delta_c\sqrt{2\pi}}e^{-\frac{\delta_H^2}{2\Delta_H^2}} \tag{2.43}$$

So, 0.8β of the collapsing matter comes to critical gravitational collapse.
The density parameter of PBH then:

$$\Omega_{BH} = \frac{\beta}{2^{2/3}}\left(\frac{3}{2\pi}\right)^{1/6}\frac{c}{M_x^{1/3}G^{1/2}\rho_{eq}^{1/6}}\frac{\Delta_H}{\delta_c}e^{-\frac{\delta_H^2}{2\Delta_H^2}} \tag{2.44}$$

So, the PBH form in the tail of the Gaussian fluctuation distribution and non-compact objects form from rms fluctuations. PBH and non-compact objects have common perturbation spectrum, but they don't form from the same fluctuations.

2.7 Conclusion

To conclude, this chapter started with the description of the adiabatic and isothermal scalar perturbations. Isothermal perturbations in cosmology refer to density fluctuations that preserve their temperature as they evolve, often associated with dark matter, while adiabatic perturbations involve fluctuations where the entropy remains constant, commonly linked to both dark matter and baryonic matter, and are essential for the formation of cosmic structures. The distinguish between these perturbations will be important in Chapter 3. In order to quantify these perturbations, we have to make use of primordial power spectrum, which is further discussed. The power spectrum resulting from scalar perturbations in cosmology describes the statistical distribution of density fluctuations as a function of their spatial scale, providing crucial information about the structure and evolution of the Universe. The derivation of the primordial power spectrum as the power-law (2.7) is shown in the Section 2.3. The next Sections 2.4, 2.5 introduced the evolution of the overdensity. The evolution of perturbations in cosmology describes how fluctuations in matter density or temperature, initially generated during the early Universe, grow and evolve under the influence of gravity and other physical processes, eventually leading to the formation of cosmic structures. The evolution of dark matter perturbations can be described by (2.33). Lastly, the Chapter discussed the formation of the primordial black holes. The threshold needed for its formation (2.34) and the fraction of the PBH formation at the equivalence period is described by (2.43) [18].

Chapter 3

Dynamics and Evolution of Dark Matter Protohalos

3.1 Introduction

Dark matter clumps, also known as dark matter halos, form in the early Universe as a result of gravitational instability and the amplification of initial density fluctuations. These fluctuations originated from quantum fluctuations during the inflationary epoch and were imprinted in the fabric of spacetime. The overdense regions of dark matter attract more matter into this region resulting in the collapse and eventual formation of dark matter protohalo. The reason to call it protohalo is because the actual formation of the dark matter halo happens when the overdense region becomes locally matter dominated. The dynamics of the formation of this dense object is mathematically sophisticated. First, we consider a simple case, spherical collapse, which can result from isocurvature perturbations or adiabatic ones. Section 3.2 presents fully developed calculations of the dynamics of the spherical collapse from the isocurvature fluctuations. Section 3.3 presents the calculations for adiabatic perturbations that results in the spherical collapse. Both sections allow us to see how the region evolves to form ultradense dark matter clump. In Section 3.4, a more sophisticated case is considered, ellipsoidal collapse. In this case, it is possible to take into account non-radial evolution of the region, since in reality the collapsing object is more like an ellipsoid. Section 3.5 introduces the dynamics of the formation of the ultradense dark matter halo with the specified overdensity growth. This density growth accounts for the ellipsoidal shape of the halo.

3.2 Spherical Collapse for Isocurvature Perturbations

3.2.1 Equation of Motion

Consider an overdense region of radius r containing dust in a flat Universe in the radiation dominated epoch. The equation of motion (EOM) for the radius r of the region:

$$\ddot{r} = -\frac{8\pi G}{3}\rho_R r - \frac{GM_{tot}}{r^2} \tag{3.1}$$

where M_{tot} is the total mass of matter contained in the region of radius r.

Let's change to conformal time coordinate $d\eta = \frac{dt}{a(t)}$. Start with the right hand side of the Equation 3.1. We change the variables, $\frac{d}{dt} = \frac{1}{a}\frac{d}{d\eta}$:

$$\frac{d}{dt}\left(\frac{d}{dt}r\right) = \frac{1}{a}\frac{d}{d\eta}\left(\frac{1}{a}\frac{d}{d\eta}r\right) = \frac{1}{a}\left(-\frac{da}{d\eta}\frac{dr}{d\eta}\frac{1}{a^2} + \frac{1}{a}\frac{d^2r}{d\eta^2}\right) = -\frac{1}{a^3}a'r' + \frac{1}{a^2}r'' \tag{3.2}$$

The left hand side stays the same, the equation becomes:

$$\frac{1}{a^2}r'' - \frac{1}{a^3}a'r' = -\frac{8\pi G}{3}\rho_R r - \frac{GM_{tot}}{r^2} \tag{3.3}$$

Multiplying by a^3:

$$ar'' - a'r' = -\frac{8\pi G}{3}\rho_R r a^3 - \frac{GM_{tot}}{r^2}a^3 \tag{3.4}$$

Rewrite the EOM in terms of co-moving reference frame,

$$r = a(\eta)R_\xi\xi \tag{3.5}$$

Start with the RHS and omit ξ subscript:

$$a\frac{d}{d\eta}\left(\frac{d}{d\eta}aR\xi\right) - a'\frac{d}{d\eta}\left(aR\xi\right) \tag{3.6}$$

First derivative gives:

$$\frac{d}{d\eta}(aR\xi) = \xi a'R + \xi aR' \tag{3.7}$$

The second derivative:

$$\frac{d}{d\eta}\left(\xi a'R + \xi aR'\right) = \xi(a''R + a'R') + \xi(a'R' + aR'') = \xi(a''R + 2a'R' + aR'') \tag{3.8}$$

Now we insert 3.7, 3.8 into 3.6:

$$a\xi(a'' + 2a'R' + aR'') - \xi(a'^2R + aa'R') = \tag{3.9}$$
$$= \xi(aa''R + 2aa'R' + a^2R'' - a'^2R - aa'R') = \tag{3.10}$$
$$= \xi(a^2R''aa'R' + R(aa'' - a'^2)) \tag{3.11}$$

where we use the Friedmann equations to express $aa'' - a'^2$.

$$aa'' - a'^2 = \frac{4\pi G}{3}\rho_M a^4 - \frac{8\pi G}{3}(\rho_M + \rho_R)a^4 = -\frac{4\pi G}{3}\rho_M a^4 - \frac{8\pi G}{3}\rho_R a^4 \tag{3.12}$$

So the LHS becomes:

$$a\xi(aR'' + a'R') - \xi R\frac{4\pi G}{3}\rho_M a^4 - \xi R\frac{8\pi G}{3}\rho_R a^4 \tag{3.13}$$

Now, the RHS becomes:

$$-\frac{8\pi G}{3}\rho_R r a^3 - \frac{GM_{tot}}{r^2}a^3 = -\frac{8\pi G}{3}\rho_R\xi R a^4 - \frac{GM_{tot}}{R^2\xi^2}a \tag{3.14}$$

Now, let's combine 3.13 with 3.14:

$$a\xi(aR'' + a'R') - \xi R\frac{4\pi G}{3}\rho_M a^4 - \xi R\frac{8\pi G}{3}\rho_R a^4 = -\frac{8\pi G}{3}\rho_R\xi R a^4 - \frac{GM_{tot}}{R^2\xi^2}a \tag{3.15}$$

The EOM becomes:

$$aR'' + a'R' + \left(-\frac{4\pi G}{3}\rho_M R a^3 + \frac{GM_{tot}}{R^2\xi^3} \right) = 0 \tag{3.16}$$

The scale factor of this region satisfies Einstein Equations in a flat, radiation dominated Universe containing pressureless matter. The Friedmann Equations:

$$\ddot{a} = -\frac{4\pi G}{3}a(\rho_R + \rho_M) \tag{3.17}$$

$$\dot{a}^2 = \frac{8\pi G}{3}a^2(\rho_R + \rho_M) \tag{3.18}$$

Again, we change to the conformal time coordinate, $\frac{d}{dt} = \frac{1}{a}\frac{d}{d\eta}$, the second derivative:

$$\frac{d}{dt}\left(\frac{d}{dt}a\right) = \frac{1}{a}\frac{d}{d\eta}\left(\frac{1}{a}\frac{d}{d\eta}a\right) = \frac{1}{a}\frac{a''a - a'^2}{a^2} = \frac{a''}{a^2} - \frac{a'^2}{a^3} \tag{3.19}$$

And the first derivative:

$$\dot{a} = \frac{a'}{a} \tag{3.20}$$

Now, we insert it into :

$$\frac{a''}{a^2} - \frac{a'^2}{a^3} = -\frac{4\pi G}{3}a(\rho_R + \rho_M) \tag{3.21}$$

$$\left(\frac{a'}{a}\right)^2 = \frac{8\pi G}{3}(\rho_R + \rho_M)a^2 \tag{3.22}$$

Rearranging the equations:

$$\frac{a''}{a^3} - \frac{a'^2}{a^4} = -\frac{4\pi G}{3}\rho_M \tag{3.23}$$

$$\frac{a'^2}{a^4} = \frac{8\pi G}{3}(\rho_R + \rho_M) \tag{3.24}$$

$$\frac{a''}{a^3} = -\frac{4\pi G}{3}(\rho_R + \rho_M) + \frac{a'^2}{a^4} = \tag{3.25}$$

$$= -\frac{4\pi G}{3}(\rho_R + \rho_M) + \frac{8\pi G}{3}(\rho_R + \rho_M) = \tag{3.26}$$

$$= \frac{4\pi G}{3}(\rho_R + \rho_M) \tag{3.27}$$

So, in conformal time coordinate:

$$a'' = \frac{4\pi G}{3}\rho_M a^3 \tag{3.28}$$

$$a'^2 = \frac{8\pi G}{3}(\rho_R + \rho_M)a^4 \tag{3.29}$$

The energy densities can be expressed in terms of the energy densities at the equivalence moment, when radiation and matter are equally spread in the universe.

$$\rho_M = \rho_{EQ}\left(\frac{a_{EQ}}{a}\right)^3 \qquad\qquad \rho_R = \rho_{EQ}\left(\frac{a_{EQ}}{a}\right)^4 \tag{3.30}$$

We obtain the following equation:

$$a'' - \frac{1}{2a}a'^2 = 0 \tag{3.31}$$

With the solution is:

$$a(\eta) = \left(2\frac{\eta}{\eta_*} + \left(\frac{\eta}{\eta_*}\right)^2\right)a_{EQ} \tag{3.32}$$

where

$$\frac{1}{\eta_*^2} = \frac{2\pi G\rho_{EQ}}{3}a_{EQ}^2 \tag{3.33}$$

Parametrizing the total mass M_{tot} in the region in terms of the excess density compared to the background one, $\Phi(\xi) = \frac{\delta\rho_M}{\rho_M}$,

$$\rho = \rho_M + \delta\rho_M = \rho_M(1+\Phi) = \rho_{EQ}\frac{a_{EQ}^3}{a^3}(1+\Phi) \tag{3.34}$$

The mass is given as follows, we express it in terms of co-moving reference frame and excess density parameter:

$$M_{tot} = \frac{4\pi}{3}\rho r^3 = \frac{4\pi}{3}\rho_{EQ}\frac{a_{EQ}^3}{a^3}(1+\Phi)(aR\xi)^3 \tag{3.35}$$

So, we obtain:

$$M_{tot} \equiv \frac{4\pi}{3}\rho_{EQ}a_{EQ}^3\big(1+\Phi\big)\xi^3 \tag{3.36}$$

Now we perform a change of variable from η to $x \equiv \frac{a}{a_{EQ}}$. First let's express it in terms of the new variable x.

$$x = 2\frac{\eta}{\eta_*} + \left(\frac{\eta}{\eta_*}\right)^2 \tag{3.37}$$

Let's find the derivative:

$$\frac{dx}{d\eta} = \frac{2}{\eta_*} + 2\frac{\eta}{\eta_*^2} = \frac{2}{\eta_*}\left(1+\frac{\eta}{\eta_*}\right) \tag{3.38}$$

And from the chain rule:

$$\frac{d}{d\eta} = \frac{2}{\eta_*}\left(1+\frac{\eta}{\eta_*}\right)\frac{d}{dx} \tag{3.39}$$

Let's start with the expression $aR'' + a'R'$, the first term:

$$aR'' = a\frac{a_{EQ}}{a_{EQ}}R'' = xa_{EQ}\frac{2}{\eta_*}\left(1+\frac{\eta}{\eta_*}\right)\frac{d}{dx}\left(\frac{2}{\eta_*}\left(1+\frac{\eta}{\eta_*}\right)\frac{dR}{dx}\right) = \tag{3.40}$$

$$= a_{EQ}x\left(\frac{2}{\eta_*}\right)^2\left(1+\frac{\eta}{\eta_*}\right)\left(\frac{1}{\eta_*}\frac{d\eta}{dx}\frac{dR}{dx} + \left(1+\frac{\eta}{\eta_*}\right)\frac{d^2R}{dx^2}\right) \tag{3.41}$$

Let's insert the following expression:

$$\frac{d\eta}{dx} = \frac{\eta_*}{2}\left(1+\frac{\eta}{\eta_*}\right)^{-1} \tag{3.42}$$

And we get:

$$a_{EQ}x\left(\frac{2}{\eta_*}\right)^2\left(1+\frac{\eta}{\eta_*}\right)\left(\frac{1}{2}\left(1+\frac{\eta}{\eta_*}\right)^{-1}\frac{dR}{dx}+\left(1+\frac{\eta}{\eta_*}\right)\frac{d^2R}{dx^2}\right)= \tag{3.43}$$

$$=a_{EQ}x\left(\frac{2}{\eta_*}\right)^2\left(\frac{1}{2}\frac{dR}{dx}+\left(1+\frac{\eta}{\eta_*}\right)^2\frac{d^2R}{dx^2}\right) \tag{3.44}$$

If we open the following expression, we can rewrite it using (3.32):

$$\left(1+\frac{\eta}{\eta_*}\right)^2=1+2\frac{\eta}{\eta_*}+\left(\frac{\eta}{\eta_*}\right)^2=1+x \tag{3.45}$$

Now, let's focus on the second term:

$$a'R'=a_{EQ}\frac{2}{\eta_*}\left(1+\frac{\eta}{\eta_*}\right)\frac{d(a/a_{EQ})}{dx}\frac{2}{\eta_*}\left(1+\frac{\eta}{\eta_*}\right)\frac{dR}{dx}= \tag{3.46}$$

$$=a_{EQ}\left(\frac{2}{\eta_*}\right)^2\left(1+\frac{\eta}{\eta_*}\right)^2\frac{dR}{dx}=a_{EQ}\left(\frac{2}{\eta_*}\right)^2(1+x)\frac{dR}{dx} \tag{3.47}$$

Now, let's sum both terms:

$$a_{EQ}x(1+x)\left(\frac{2}{\eta_*}\right)^2\frac{d^2R}{dx^2}+a_{EQ}x\left(\frac{2}{\eta_*}\right)^2\frac{1}{2}\frac{dR}{dx}+a_{EQ}\left(\frac{2}{\eta_*}\right)^2(1+x)\frac{dR}{dx}= \tag{3.48}$$

$$=a_{EQ}\left(\frac{2}{\eta_*}\right)^2\left(x(1+x)\frac{d^2R}{dx^2}+(1+\frac{3}{2}x)\frac{dR}{dx}\right)= \tag{3.49}$$

$$=4\frac{2\pi G\rho_{EQ}}{3}a_{EQ}^3\left(x(1+x)\frac{d^2R}{dx^2}+(1+\frac{3}{2}x)\frac{dR}{dx}\right) \tag{3.50}$$

Now, let's see the other part of the equation with the change of variables and some rearrangements:

$$-\frac{4\pi G}{3}\rho_M Ra^3+\frac{GM_{tot}}{R^2\xi^3}= \tag{3.51}$$

$$=-\frac{4\pi G}{3}\rho_{EQ}\left(\frac{a_{EQ}}{a}\right)^3Ra^3+\frac{G}{R^2\xi^3}\left(\frac{4\pi}{3}\rho_{EQ}a_{EQ}^3\big(1+\Phi\big)\xi^3\right)= \tag{3.52}$$

$$=\frac{4\pi G}{3}\rho_{EQ}a_{EQ}^3\left(\frac{1+\Phi}{R^2}-R\right) \tag{3.53}$$

When combining both parts some coefficients cancel and we obtain the following equation:

$$x(1+x)\frac{d^2R}{dx^2}+(1+\frac{3}{2}x)\frac{dR}{dx}+\frac{1}{2}\left(\frac{1+\Phi}{R^2}-R\right)=0 \tag{3.54}$$

If we assume that the deviation of the shell motion from the background cosmological expansion is very small, $R\equiv 1-\delta$ with $\delta\ll 1$, then we can reduce the Equation 3.54 to Meszaros equation:

$$x(1+x)\frac{d^2\delta}{dx^2}+(1+\frac{3}{2}x)\frac{d\delta}{dx}-\frac{3}{2}\delta=0 \tag{3.55}$$

The analytic solution is $\delta=\delta_0(1+\frac{3x}{2})$ which is the growing mode of the equation.
Numerical solution to the Equation 3.54 at the limit $x_0\ll 1$, with $R(x_0)=1$ gives us

$$R=(1-\frac{3}{2}\Phi x)^{1/3}\simeq 1-\frac{1}{2}\Phi x \tag{3.56}$$

taking into account that the second derivative is negligible at early times, we can perform the approximation as well.

The solution can be approximated analytically, resulting in:

$$R(x) = 1 - \frac{\Phi x}{2} - \frac{\Phi^2 x^2}{8} - \frac{(8\Phi^3 - \Phi^2)x^3}{144} \tag{3.57}$$

R describes the deviation of the shell motion from the Hubble flow, in other words, it describes how much the overdense region is denser than the uniform background. So, the solution describes the time evolution of the overdensity. At a given time, x, we can identify how the region will be different from the uniform background. It can be defined as $R = 1 - \delta$, meaning that $R = 1$ corresponds to the uniform background, where δ is the overdensity of the region.

3.2.2 Parameters of the Overdense Region

Now, let's analyze the parameters of this overdense region, in particular, its radius and density at the maximum point or otherwise known as turnaround point. This turnaround point is characterized by $\dot{r} = 0$, since the expansion stops for a moment before collapsing. After the turnaround point, the system gets stabilized in the radius half of the turnaround radius and hence the final density is 8 times larger than the density at the turnaround point. Taking into account this we can say that $R_{TA} = const$ and $x_{TA} = \frac{const}{\Phi}$.

The density is given by

$$\rho_{TA} = \frac{1}{4\pi r^2}\frac{dM}{dr} \tag{3.58}$$

with $r = R_{TA}x_{TA}\xi$.

As a result, the parameters at the turnaround:

$$x_{TA} = \frac{C_x}{\Phi} \qquad\qquad \rho_{TA} = C_\rho \rho_{EQ}\frac{\Phi^3}{3\xi^2}\frac{d}{d\xi}(1+\Phi)\xi^3 \tag{3.59}$$

The coefficients C_x, C_ρ are obtained numerically. And the final density is found to be:

$$\rho_F \simeq 140\rho_{EQ}\frac{\Phi^3}{3\xi^2}\frac{d}{d\xi}(1+\Phi)\xi^3 \tag{3.60}$$

3.3 Spherical Collapse for Adiabatic Perturbations

The equation of motion for the adiabatic perturbations:

$$y(1+y)\frac{d^2b}{dy^2} + \left(1 + \frac{3}{2}y\right)\frac{db}{dy} + \frac{1}{2}\left(\frac{1}{b^2} - b\right) = 0 \tag{3.61}$$

where $y = a(\eta)/a_{eq}$ with parametrization. This Equation was derived in the same way as (3.54).

$$r = a(\eta)b(\eta)\xi \tag{3.62}$$

where ξ is the comoving coordinate and $b(\eta)$ allows deceleration of cosmological expansion.

Expressing it in terms of δ:

$$b = (1+\delta)^{-1/3} \tag{3.63}$$

The evolution of the adiabatic perturbation, δ, in the radiation dominated stage can be seen from the Figure 3.1.

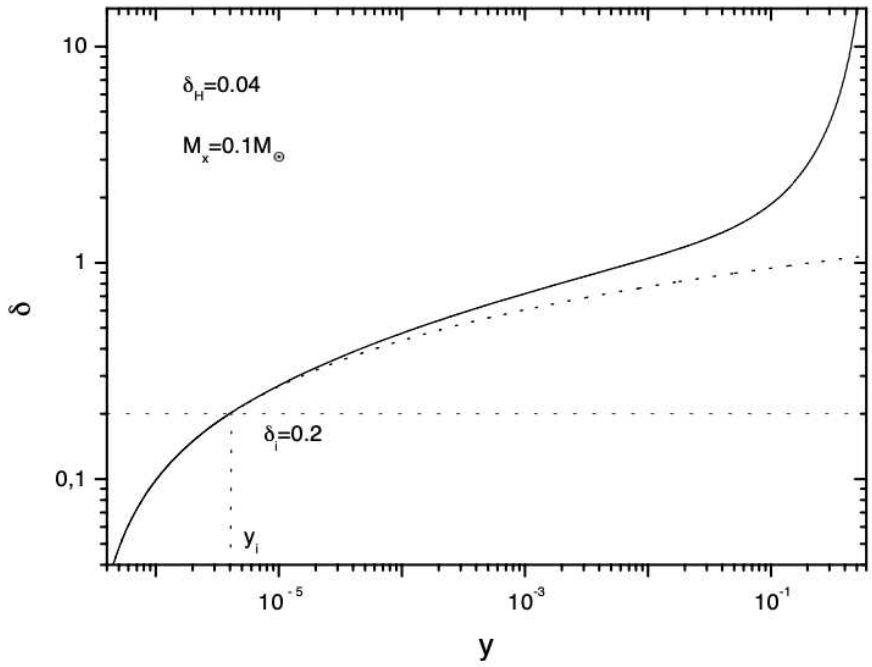

Figure 3.1: Evolution of the perturbation at the radiation dominated epoch. Here $y = a/a_{eq}$, [18].

For entropic (isocurvature) pertubations the initial velocity can be neglected, since it doesn't affect the result, $db/dy \simeq 0$. However, for adiabatic perturbations the initial velocity is quite high. Therefore the solution to the Equation 3.61 in the limit of $x \gg 1$ and $y \ll 1$ is:

$$x = \frac{\pi}{2^{2/3}} \left(\frac{3}{2\pi}\right)^{1/6} \frac{yc}{M_x^{1/3} G^{1/2} \rho_{eq}^{1/6}} \tag{3.64}$$

The initial conditions are $b_i = (1 + \delta_i)^{-1/3}$ at y_i and using 2.15, 3.63 and 3.64, we obtain:

$$\frac{db}{dy} = -\frac{b}{y} \tag{3.65}$$

3.3.1 Parameters of the overdense region

So, at the maximum point or otherwise called turnaround point, we have the following parameters:

$$\rho_{max} = \rho_{eq} y_{max}^{-3} b_{max}^{-3} \qquad R_{max} = \left(\frac{3M_x}{4\pi\rho_{max}}\right)^{1/3} \tag{3.66}$$

This means that we can calculate the parameters for the region for a specified perturbation value δ, if it is in the limit $\delta \ll 1$.

3.4 Ellipsoidal Collapse

3.4.1 Formalism

Spherical collapse can account for radial motion only within an expanding overdense region. The simplest way to treat non-radial option is to consider ellipsoidal model of collapse. Reference [33] summarizes the ellipsoidal model formalism.

The surface of the ellipsoid is described with:

$$\frac{x^2}{a^2} + \frac{y^2}{b^2} + \frac{z^2}{c^2} = 1 \tag{3.67}$$

where x, y, z are Cartesian coordinates and a, b, c are semi-axes of the ellipsoid.

The gravitational potential inside the ellipsoid is:

$$\Phi = \pi G\rho\big(Ax^2 + By^2 + Cz^2\big) \tag{3.68}$$

where the coefficients are:

$$A = abc\int_0^\infty \frac{d\lambda}{(a^2+\lambda)f^{1/2}} \tag{3.69}$$

$$B = abc\int_0^\infty \frac{d\lambda}{(b^2+\lambda)f^{1/2}} \tag{3.70}$$

$$C = abc\int_0^\infty \frac{d\lambda}{(c^2+\lambda)f^{1/2}} \tag{3.71}$$

and the function f is defined as:

$$f = (a^2+\lambda)(b^2+\lambda)(c^2+\lambda) \tag{3.72}$$

The coefficients sum up as:

$$A + B + C = 2 \tag{3.73}$$

giving the hint on the fact that the potential of the ellipsoid satisfies the Poisson's equation.

$$\nabla^2\phi = 4\pi G\rho(t) \tag{3.74}$$

If the motion is homogeneous we can set a linear relation between the proper position r^α and the coordinate x^α in the following way:

$$r^\alpha = S^{\alpha\beta}(t)x^\beta \tag{3.75}$$

where S is a function of time. The potential of the ellipsoid can be written as

$$\phi = \frac{1}{2}\Phi_{\alpha\beta}(t)r^\alpha r^\beta \tag{3.76}$$

The acceleration of the fluid element is then

$$\frac{d^2r^\alpha}{dt^2} = \frac{d^2S^{\alpha\beta}}{dt^2}x^\beta = -\Phi_{\alpha\beta}r^\beta \tag{3.77}$$

which can be rewritten as:

$$\frac{d^2S^{\alpha\beta}}{dt^2} = -\Phi_{\alpha\gamma}S^{\gamma\beta} \tag{3.78}$$

3.4.2 Small Deviation from Spherical Shape

To take into account the evolution of non-spherical layers Reference [4] suggests to consider small deviations (σ) from the spherical case and consider a homogeneous ellipsoid. The total potential of the perturbation is

$$\Phi = \Phi_{el} + \Phi_{bg} + \Phi_{sh} \tag{3.79}$$

which are potentials of ellipsoid, background and tidal forces. The potential for the homogeneous background reads as:

$$\Phi_{bg} = 4\pi G\bar{\rho}(t)\frac{I}{3} \tag{3.80}$$

where I is the unit matrix.

The evolution of the non-spherical region can be described by the equation (number). We can express the matrix of the ellipsoid S as

$$S = \left\| \begin{matrix} a & & \\ & b & \\ & & c \end{matrix} \right\| = Ir + \sigma \tag{3.81}$$

And the potential of the ellipsoid can be rewritten as:

$$\Phi_{el} = 2\pi G\rho_e \left\| \begin{matrix} A & & \\ & B & \\ & & C \end{matrix} \right\| \tag{3.82}$$

where the coefficients were defined in the previous section (put reference here) and the density of the ellipsoid is given by:

$$\rho_e \equiv \frac{M_e}{V} = \rho_m\left(\frac{1+\delta_i}{b^3} - 1\right) \tag{3.83}$$

Define $\Delta = Tr(\sigma)$ and expand the potential of the ellipsoid to the linear order in σ for $\sigma \ll 1$ as

$$\Phi_{el} = 2\pi G\rho_e\left(\frac{2}{3}\left(1 + \frac{2}{5}\frac{\Delta}{r}\right)I - \frac{4}{5}\frac{\sigma}{r}\right) \tag{3.84}$$

For the zero order in $\sigma = 0$, we restore the equation (number). But to the linear order in σ we have

$$\frac{d^2\sigma}{dt^2} = \frac{4\pi}{15}G\rho_e\sigma - \frac{4\pi}{3}G(2\rho_e + \rho_m)\sigma \tag{3.85}$$

We parametrize $\sigma = a(y)s(y)\xi$, so that the equation for the new function $s(y)$ can be written as

$$y(y+1)s'' + \left(1 + \frac{3}{2}y\right)s' - \frac{1}{10}\left(\frac{1}{b^3} - 1\right)s = 0 \tag{3.86}$$

The initial conditions for the homogeneous ellipsoid at the radiation dominated epoch in the conformal Newtonian frame with scale $r \gg ct$, we have:

$$\delta_r = -2\Phi = const \tag{3.87}$$

$$\delta_i = \frac{3}{4}\delta_{r,i} = -\frac{3}{2}\Phi_i \tag{3.88}$$

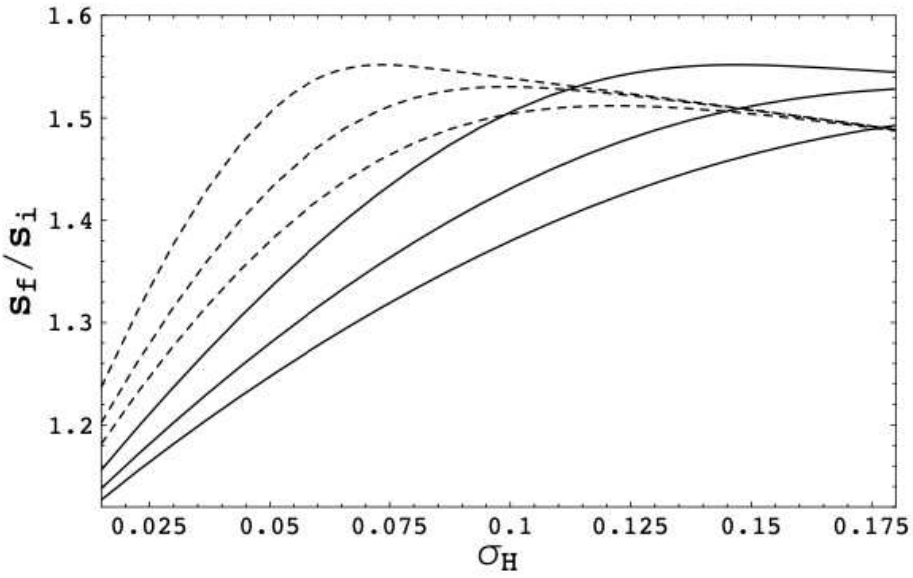

Figure 3.2: The growth of asphericity with respect to the rms perturbation at the horizon crossing, [4].

The solution of the relativistic potential is

$$\Phi(\eta, \vec{k}) = \Phi_i(\vec{k}) \frac{3\pi^{1/2}}{2^{1/2}(u_s k\eta)^{3/2}} J_{3/2}(u_s k\eta) \tag{3.89}$$

where $u_s = \frac{1}{\sqrt{3}}$.

The peculiar velocities v_j, which define the initial velocity of the ellipsoid's surface, can be written as $v_j = \frac{\partial v}{\partial x_j}$, where the velocity potential is written as

$$v(\vec{k}) = -\frac{1}{\eta} \int_0^\eta d\eta' \eta' \Phi(\eta', \vec{k}) = -9\Phi_i(\vec{k}) \frac{1}{\eta k^2} \tag{3.90}$$

The form of the ellipsoidal top-hat perturbation depends on the following condition, if $\frac{x^2}{a^2} + \frac{y^2}{b^2} + \frac{z^2}{c^2} \leq 1$, then the perturbation is constant, $\delta_i(\vec{x}) = \delta_i$, otherwise, $\delta_i(\vec{x}) = 0$.

Approximating the velocity potential for a small non-sphericity, we can obtain:

$$v = v_0 + \left.\frac{\partial v}{\partial a}\right|_0 \Delta a + \left.\frac{\partial v}{\partial b}\right|_0 \Delta b + \left.\frac{\partial v}{\partial c}\right|_0 \Delta c + ... \tag{3.91}$$

where zero corresponds to the spherical case with $a = b = c$. So, the initial conditions in this case for each component is in the form:

$$s|_{y_i} = s_i \qquad\qquad s'|_{y_i} = \frac{3\delta_H b_i^3 s_i}{10 y_i \phi} \tag{3.92}$$

The equations 3.61 and 3.86 has to be solved numerically simultaneously for peaks as high as $\nu = 1$ and $\nu = 2$, which is defined as $\nu \equiv \delta_H/\sigma_H$ and $\sigma_H \equiv < \delta_H^2 >^{1/2}$. The new function $s(y)$ measures how much the non-spherical shell deviates from the spherical shape. So, we can relate it to the asphericity. From [4] we have results for the solution to the equations 3.61,3.86, they have arrived to the conclusion that the asphericity growth, which can be quantified as $\frac{s_f}{s_i}$ grow with the rms perturbation value at the horizon crossing,

σ_H, increasing with the increase of the mass of the forming clump. The results can be seen in the Figure 3.2. For the case of isocurvature perturbations with $s'(t_i) = 0$, the asphericity growth is small. In the curvature perturbations, the boundary of the allowed asphericity for the formation of superdense dark matter clump in the radiation domination era is

$$\frac{\Delta s_i}{b_i} < \frac{b_f}{b_i}\frac{\Delta s_i}{\Delta s_f} \tag{3.93}$$

The ellipticity of the potential of the ellipsoidal distribution can be expressed as

$$e = \frac{\lambda_1 - \lambda_2}{2\sum \lambda_i} \simeq \frac{1}{5}\frac{\Delta s_i}{b_i} \tag{3.94}$$

where λ_i are the eigenvalues of the gravitational shear tensor.
The prolateness is written as

$$p = \frac{\lambda_1 + \lambda_3 - 2\lambda_2}{\sum \lambda_i} \tag{3.95}$$

The distribution over the eigenvalues $\lambda_1 \geq \lambda_2 \geq \lambda_3$ can be reprepsented in the following form followed by [19]

$$p(\lambda_1, \lambda_2, \lambda_3) = \frac{15^3}{8\pi\sqrt{5}\sigma^6} \exp\left(-\frac{3I_1^2}{\sigma^2} + \frac{15I_2}{2\sigma^2}\right)(\lambda_1 - \lambda_2)(\lambda_2 - \lambda_3)(\lambda_1 - \lambda_3) \tag{3.96}$$

here σ is the rms perturbation and I_i are defined as

$$I_1 = \lambda_1 + \lambda_2 + \lambda_3 \tag{3.97}$$

$$I_2 = \lambda_1\lambda_2 + \lambda_2\lambda_3 + \lambda_1\lambda_3 \tag{3.98}$$

This distribution can be described with ellipticity and prolateness as, [36]

$$g(e, p|\nu) = \frac{1125}{\sqrt{10\pi}} e(e^2 - p^2)\nu^5 e^{-\frac{5}{2}\nu^2(3e^2+p^2)} \tag{3.99}$$

where $\nu \equiv \frac{\delta}{\sigma}$. This distribution was integrated over p in the range $-e < p < e$ to be used by [4] in order to compute the fraction of the formed dark matter clumps. The results are presented in Figure 3.3. The figure represents the fraction of clumps, f_{cl}, which formed by surviving the growth of anisotropy, from which we can conclude that asphericity reduces the number of formed clumps significantly, where σ_H is the rms fluctuation at the horizon crossing.

The fact that the fraction of survived clumps is so small depends also on the following mechanism. The absolute value of s doesn't grow much, hence $\frac{s_f}{s_i}$ is not significant. Whereas the relative asphericity growth is noticable due to the fact that $\frac{b_i}{b_f}$ itself is quite large. In [4], they have plotted the ratio of s_f/b_f and s_i/b_i, which is shown in Figure 3.4. From which we can conclude that the initial asphericity (s_i/b_i) has to be very small in order for the final asphericity to fit the limit of $s_f/b_f > 1$. This is why the distribution of asphericity in Eq.3.99 gives such a strong suppression of f_{cl}.

3.5 Formation of Ultradense Dark Matter Halos

During radiation dominated epoch, primordial curvature perturbations ζ at the scale wavenumber k cause linear order dark matter density perturbations to grow as

$$\delta(k, a) = I_1\zeta(k)\log\left(I_2 a/a_H\right) = I_1\zeta(k)\log\left(\sqrt{2}I_2\frac{k}{k_{eq}}\frac{a}{a_{eq}}\right) \tag{3.100}$$

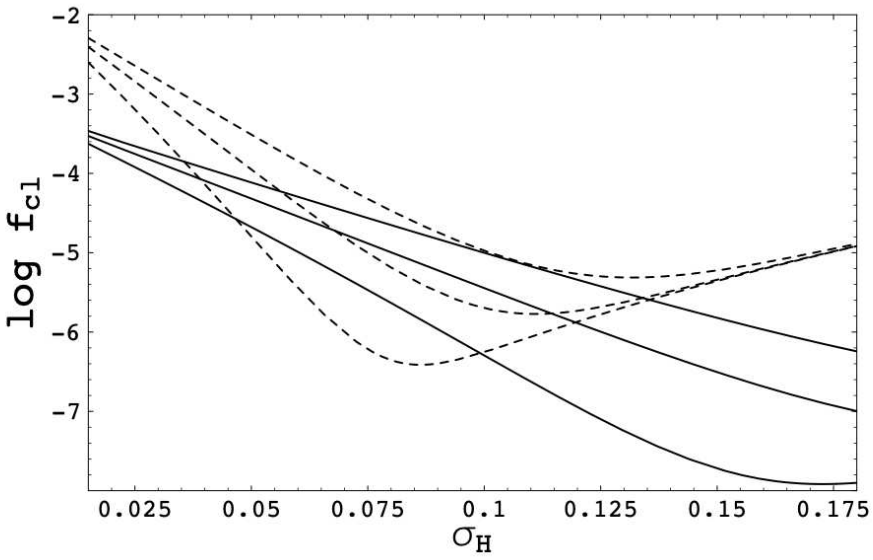

Figure 3.3: Fraction of clumps f_{cl} for peaks $\nu = 1$ (solid line) and $\nu = 2$ (dashed line) for clump masses $M = 10^2, 10^{-1}, 10^{-6} M_\odot$ (from up to down), [4].

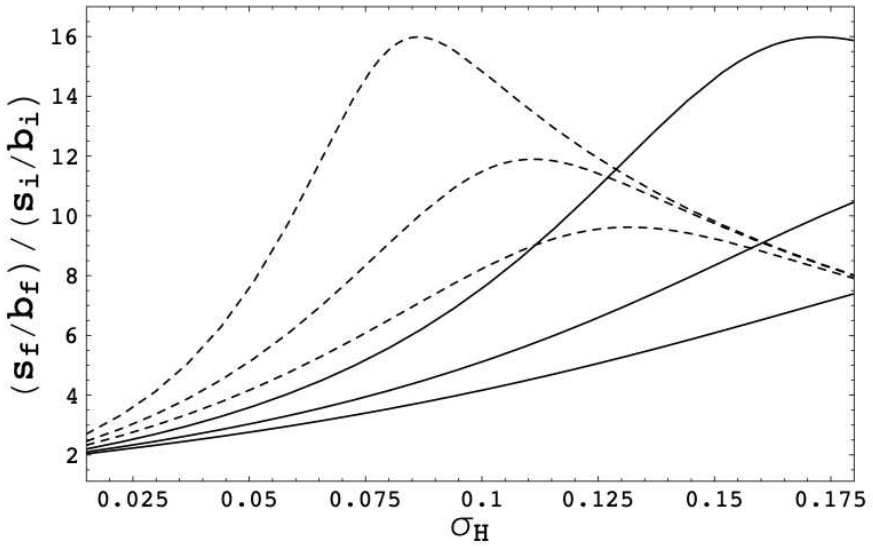

Figure 3.4: Relative asphericity $(s_f/b_f)/(s_i/b_i)$ for peaks $\nu = 1$ (solid line) and $\nu = 2$ (dashed line) for clump masses $M = 10^2, 10^{-1}, 10^{-6} M_\odot$ (from up to down), [4].

when $a \gg a_H$, where $a_H = 2^{-1/2}(k_{eq}/k)a_{eq}$ is the expansion scale factor at horizon entry, $I_1 \simeq 6.4$ and $I_2 \simeq 0.47$. The expansion factor and horizon scale the matter-radiation equality are $a_{eq} \simeq 3 \times 10^{-4}$ and $k_{eq} \simeq 0.01\text{Mpc}^{-1}$. The growth described by this Equation 3.100 arises from unaccelerated particle drift, in which particles cover comoving distances logarithmic in a. The particles are initially set in motion by the transient peculiar potential at horizon entry, before the radiation pressure homogenizes it. The application of this Eq.3.100 assumes that the dark matter is nonrelativistic and decoupled from the radiation during this horizon entry gravitational kick.

The peculiar gravitational forces are negligible, therefore the ellipsoidal collapse treatment simplifies a lot. If a region of scale k^{-1} has an initial tidal field with ellipticity e and prolateness p, then its density evolves as

$$\frac{\rho}{\rho_m} = \frac{1}{|1-\lambda_1\delta(k,a)|}\frac{1}{|1-\lambda_2\delta(k,a)|}\frac{1}{|1-\lambda_3\delta(k,a)|} \tag{3.101}$$

where ρ_m is the average dark matter density and the parameters λ_i are

$$\lambda_1 = \frac{1+3e+p}{3} \qquad \lambda_2 = \frac{1-2p}{3} \qquad \lambda_3 = \frac{1-3e+p}{3} \tag{3.102}$$

Each axis is allowed to drift independently, the last axis collapses at the critical scale factor, a_c, when $\lambda_3\delta(k,a_c) = 1$, leading to critical density contrast

$$\delta_c = \frac{3}{1-3e+p}. \tag{3.103}$$

For a density contrast δ in a Gaussian random density field with rms contrast σ, the most probable values of e and p are, [36]

$$e = \frac{\sigma}{\sqrt{5}\delta} \qquad\qquad p = 0 \tag{3.104}$$

A typical 3σ density peak has a collapse threshold of about $\delta_c \simeq 5$. This peak requires $\zeta \gtrsim 0.5$ to collapse by $a \simeq 10a_H$. However, only $\zeta \gtrsim 0.15$ is needed to ensure the collapse by $a \simeq 300a_H$. For a primordial black hole $\zeta \sim 1$, which means that the ultradense halos outnumber primordial black holes a lot.

The formation of halos from collapsed protohalo cannot be ensured until the local region becomes matter dominated, only then the protohalo becomes virialized and actually forms a halo. This was shown in the simulation in the work [5]. For the typical ellipticity $e \simeq 0.15$ of the tidal field at a 3σ peak, local matter domination occurs at $a \sim e^2 a_{eq} \simeq 0.02a_{eq}$, leading to halo formation long before the matter dominated epoch begins. Being proportional to the mean cosmic density at their formation time, the density inside these halos would be extraordinarily high.

Note that halo formation from isocurvature perturbations during the radiation epoch is more favorable than PBH formation. In case of adiabatic curvature perturbations, halos are less likely to form compared to PBHs, since the peculiar gravitational forces become significant prior to the local matter domination of a collapsed region [25].

3.6 Conclusion

In conclusion, this chapter examines the formation of a dark matter protohalo in the simple spherical collapse scenario and in a more realistic case of ellipsoidal collapse. The calculation starts with consideration of an overdense region in the radiation dominated

epoch, which obeys the EOM (3.1). After some mathematical manipulations, we can modify the EOM and express it in terms of the overdensity of the region and see how it evolves (3.55).

Having solved the equation numerically taking into account the nature of the perturbations, it is possible to analyze the parameters of the overdense regions, which are presented in the Section 3.2.2 [25]. Evolution of adiabatic equation is described by an analogous equation (3.61), however the solution differs due to the fact that for the adiabatic perturbations we have to take into account the initial velocity (3.65). The parameters of this scenario are specified in the Section 3.3.1 [18].

To consider a more realistic scenario, we have to take into account non-radial evolution, which can be done with the help of ellipsoidal collapse. This can be done by considering a small deviation from the spherical scenario described by (3.86). Figure 3.2 shows the dependence of the asphericity and the rms perturbations. Asphericity parameter has limits, since exceeding certain level of asphericity makes it impossible to form a halo (3.93) [4].

Chapter 4

Formation of Dark Matter Halos

4.1 Introduction

Dark matter halos form through two primary mechanisms: hierarchical clustering and gravitational attraction. These mechanisms operate during different cosmic epochs and contribute to the formation of structures at various scales in the Universe. Dark matter halos that form via gravitational attraction belong to the matter dominated epoch. Whereas dark matter halos formed via hierarchical clustering start growing structures in the radiation dominated epoch, but actually form when their region become locally matter dominated. The resulting compact object is a seed that will experience more matter accreting onto it in the matter dominated Universe, after the time of equivalence. So, it is not completely true that dark matter halos form just at the radiation epoch, rather it is a more complicated scenario. Section 4.2 focuses on the dark matter halos formation via gravitational attraction, considering only the simple case, spherical collapse. Section 4.3 considers the mechanism of hierarchical clustering and, in fact, is a continuation of the previous chapter.

4.2 Simple model in Matter Dominated Epoch

Consider a spherical region that is denser than the background in the Einstein de Sitter Universe, flat and matter dominated, with the background density ρ_c. The evolution of this region will be independent of the background evolution.

The Friedmann equations in the parametric form for this region are:

$$R = A(1 - cos\theta) \tag{4.1}$$

$$t = B(\theta - sin\theta) \tag{4.2}$$

where R is the scale factor of the spherical region.

$$A = \frac{\Omega_{m0}}{2(\Omega_{m0} - 1)} B = \frac{\Omega_{m0}}{2H_0(\Omega_{m0} - 1)^{3/2}} \tag{4.3}$$

In this case, $\Omega_{m0} > 1$ since the density of this overdense region is higher than the background, $\rho_m > \rho_c$.

According to the parametric equations, the spherical overdense region will be expanding until $\theta = \pi$, which corresponds to $R^{max} = 2A$ then turn around to collapse, which corresponds to $R^{min} = 0$ at $\theta = 2\pi$.

$$R^{max} = 2A = \frac{\Omega_{m0}}{(\Omega_{m0} - 1)} \tag{4.4}$$

$$t^{max} = \pi B = \frac{\pi \Omega_{m0}}{2H_0(\Omega_{m0} - 1)^{3/2}} \tag{4.5}$$

Let's compare the density of the spherical region to the background density.

$$\frac{\rho}{\rho_0} = \frac{\Omega_{m0}\rho_{c0}\frac{1}{(R^{max})^3}}{\rho_{c0}\frac{1}{a^3}} = \Omega_{m0}\left(\frac{a}{R}\right)^3 \tag{4.6}$$

The scale factor of the background is $a = \left(\frac{3}{2}H_0 t\right)^{2/3}$ in the matter dominated Universe. At t_{max}:

$$a^3(t_{max}) = \left(\frac{3}{2}H_0 t_{max}\right)^{2/3} = \frac{9\pi^2}{16}\frac{\Omega_{m0}^2}{(\Omega_{m0} - 1)^3} \tag{4.7}$$

Therefore, we have:

$$\frac{\rho}{\rho_0} = \frac{9\pi^2}{16} \simeq 5.55 \tag{4.8}$$

We can see that the spherical region starts to collapse when its density is 5.55 times the density of the background.

4.2.1 Virialization

In the simplified model there is no internal pressure to stop the collapse and the region collapses to the infinite density. However, in a more realistic case, the collapse will stop without reaching the infinite density. The system will reach the point where it obeys the Virial theorem, which is the most favorable energy configuration:

$$E_k = -\frac{1}{2}E_p \tag{4.9}$$

The redshift at which the region has reached its maximum before collapse is z_{max}, and the redshift after the systems has collapsed (z_c) can be derived as:

$$\frac{1 + z_c}{1 + z_{max}} = \frac{a_{max}}{a_c} = \left(\frac{t_{max}}{t_c}\right)^{2/3} = \frac{1}{2^{2/3}} \tag{4.10}$$

The potential energy at z_{max} is the total energy of the system, since the overdense region stops at the maximum before collapsing backwards.

$$E_p = -\frac{3GM^2}{5r_{max}} \tag{4.11}$$

The physical size of the region is $r = r_{max}/2$, so when the region has collapsed, the potential energy is:

$$E_p = -\frac{3GM^2}{5r_{max}/2} = -\frac{6GM^2}{5r_{max}} \tag{4.12}$$

So, using the conservation of energy law, we can find the kinetic energy of the region after the collapse:

$$E_k = E - E_p = -\frac{3GM^2}{5r_{max}} + \frac{6GM^2}{5r_{max}} = \frac{3GM^2}{5r_{max}} \tag{4.13}$$

So,

$$E_k = -\frac{1}{2}E_p(r_{max}/2) \tag{4.14}$$

The system virialized and became stable at half of the maximum radius, $r_{max}/2$. It means that the systems has become ($\left(\frac{1}{2}\right)^3 = \frac{1}{8}$), 8 times denser than when it was at turn around point. This coresponds to:

$$R^{vir} = \frac{1}{2}R^{max}A(1 - cos\theta) = A \tag{4.15}$$

which means that after collapse $\theta > \pi$, so the solution should be $\theta = \frac{3\pi}{2}$.

$$t_{vir} = B(\frac{3\pi}{2} + 1) = \pi B(\frac{3}{2} + \frac{1}{\pi}) = t_{max}(\frac{3}{2} + \frac{1}{\pi}) \simeq 1.81t_{max} \tag{4.16}$$

The background density has decreased after the collapse by the factor of

$$\left(\frac{a_{max}}{a_{vir}}\right)^3 = \left(\frac{t_{max}}{t_{vir}}\right)^2 = \frac{1}{1.81^2} \tag{4.17}$$

This means that the density of the spherical overdense region at virialization is greater than the background density by the factor of $5.55 \times 8 \times 1.81^2 \simeq 145$. If we consider virialization moment to be the moment at $R = 0$, then $t_{vir} = 2t_{max}$, which means the background density is smaller than the overdense region by the factor of $\simeq 178$.

4.2.2 Linear perturbation approach

We can analyze the spherical collapse using linear perturbation approach. Let's expand the parametric solutions in θ:

$$R = A(1 - cos\theta) \simeq A(\frac{1}{2}\theta^2 - \frac{1}{24}\theta^4) \tag{4.18}$$

$$t = B(\theta - sin\theta) = B(\frac{1}{6}\theta^3 - \frac{1}{120}\theta^5) \tag{4.19}$$

To the first order, we have

$$R = \frac{1}{2}A\theta^2 \tag{4.20}$$

$$t = \frac{1}{6}B\theta^3 \tag{4.21}$$

At the matter domination epoch, the scale factor $R \propto t^{2/3}$, the same as the background expansion. At the turnaround, the scale factor and time:

$$R_{max} = 2A \qquad\qquad t_{max} = \pi B \tag{4.22}$$

The fractions:

$$\frac{R}{R_{max}} \simeq \frac{1}{4}\theta^2 - \frac{1}{48}\theta^4 \tag{4.23}$$

$$\frac{t}{t_{max}} = \frac{1}{\pi}\left(\frac{1}{6}\theta^3 - \frac{1}{120}\theta^5\right) \tag{4.24}$$

Using the fraction of time, rewrite:

$$\theta^3 = 6\pi\frac{t}{t_{max}} + \frac{1}{20}\theta^5 \tag{4.25}$$

Now we solve the equation iteratively, with the first guess:

$$\theta^3_{(0)} = 6\pi\frac{t}{t_{max}} \tag{4.26}$$

Second guess:

$$\theta^3_{(1)} = 6\pi\frac{t}{t_{max}} + \frac{1}{20}\left(6\pi\frac{t}{t_{max}}\right)^{5/3} \tag{4.27}$$

$$\theta_{(1)} = \left(6\pi\frac{t}{t_{max}}\right)^{1/3}\left(1 + \frac{1}{20}\left(6\pi\frac{t}{t_{max}}\right)^{2/3}\right)^{1/3} \tag{4.28}$$

Define $x \equiv \frac{6\pi t}{t_{max}}$, we get

$$\theta_{(1)} \simeq x^{1/3}(1 + \frac{1}{60}x^{2/3}) \simeq x^{1/3} + \frac{1}{60}x \tag{4.29}$$

Inserting it into the fraction of the scale factor:

$$\frac{R}{R_{max}} = \frac{1}{4}\theta^2_{(1)} - \frac{1}{48}\theta^4_{(1)} \simeq \frac{1}{4}x^{2/3}(1 - \frac{1}{20}x^{2/3}) \tag{4.30}$$

As a result,

$$\frac{R}{R_{max}} = \frac{1}{4}\left(6\pi\frac{t}{t_{max}}\right)^{2/3}\left(1 - \frac{1}{20}\left(6\pi\frac{t}{t_{max}}\right)^{2/3}\right) = R_{lin} \tag{4.31}$$

The first term describes the background evolution and the second term describes the evolution of the perturbation.

So, the density of the region:

$$\rho = \rho_{bg}(1 + \delta_{lin}) \tag{4.32}$$

Rewriting the density in terms of scale factors:

$$1 + \delta_{lin} = \frac{a^3}{R^3_{lin}}$$

$$\frac{R_{lin}}{a} = (1 + \delta_{lin})^{-1/3} \simeq 1 - \frac{1}{3}\delta_{lin}$$

Since $a = \frac{1}{4}(6\pi t/t_{max})^{2/3}$, we have

$$\frac{R_{lin}}{R_{max}} = \frac{1}{4}\left(6\pi\frac{t}{t_{max}}\right)^{2/3}\left(1 - \frac{1}{3}\delta\right) \tag{4.33}$$

And,

$$\delta = \frac{3}{20}\left(6\pi\frac{t}{t_{max}}\right)^{2/3} \tag{4.34}$$

When the overdense region reaches its maximum and starts to collapse, we have $\delta^{max}_{lin} = \frac{3}{20}(6\pi)^{2/3} \simeq 1.06$. The exact calculation predicts the density to be 5.55 times the background density. After virialization, the fluctuation becomes $\delta^{vir}_{lin} \simeq 1.686$. And the actual density at the virialized point is $\simeq 178$ times denser than the background.

4.2.3 Density Contrast Evolution

At matter dominated epoch, taking into account the smooth transition from radiation to matter domination, the density contrast expression takes the form, [21]

$$\delta(k,z) \simeq \frac{27}{2}\Phi_i(k)\frac{1+z_{eq}}{1+z}\ln\left(0.2k\eta_{eq}\right) \tag{4.35}$$

where Φ_i is the initial gravitational potential outside the horizon.

4.3 Secondary Accretion on Dark Matter Clump

At the radiation domination stage a compact seed of mass M_c was formed and it is assumed to be uniformly surrounded by dark matter. At the time long before the equivalence of matter and radiation moment, $t \ll t_{eq}$, the mass $M \gg M_c$, so the isocurvature perturbation of dark matter $\delta_i = \frac{M_c}{M}$ doesn't evolve. This comes from the solution to Meszaros equation, which is

$$\delta = \delta_i\left(1+\frac{3}{2}x\right) \tag{4.36}$$

where $x = \frac{a}{a_{eq}}$, hence $\delta \equiv \delta_i$.

The secondary accretion begins at $t \sim t_{eq}$. Since we consider isocurvature perturbations, the Hubble flow was not perturbed, which happens for adiabatic perturbations. In this case, we can approximate $5\delta/3 \longrightarrow \delta$ in the top-hat model and the threshold for the object formation changes to $\delta(t) = \tilde{\delta_c} = \left(\frac{3\pi}{2}\right)^{2/3} \approx 2.81$.

Using the solution to Meszaros equation, we can find the mass of the virialized object as a function of redshift, z:

$$M(z) = \frac{3}{2}\left(\frac{2}{3\pi}\right)^{2/3}\frac{1+z_{eq}}{1+z}M_c \approx 1.7\times10^3\left(\frac{M_c}{10^2M_\odot}\right)\left(\frac{1+z}{100}\right)^{-1}M_\odot \tag{4.37}$$

The radius of the virialized clump is

$$r_c = \frac{1}{3}\left(\frac{3}{4\pi}\right)^{1/3}\frac{M^{4/3}}{\rho_{eq}^{1/3}M_c} \simeq 3.2\left(\frac{M_c}{10^2M_\odot}\right)^{1/3}\left(\frac{100}{1+z}\right)^{4/3}pc. \tag{4.38}$$

So, using the expression for mass and the radius of the formed halo, one can find the density profile of this object and it is

$$\rho(r) = \frac{1}{4\pi r_c^2}\frac{dM(r_c)}{dr_c}\bigg|_{r_c=r} \simeq 3\times10^{-21}\left(\frac{r}{1pc}\right)^{-9/4}\left(\frac{M_c}{10^2M_\odot}\right)^{3/4}\text{g cm}^{-3} \tag{4.39}$$

However, the clusters around black holes don't have exactly this density profile, $\rho \propto r^{-9/4}$. So, ultradense dark matter halos can form around a dark matter clump, which acts as a seed and was formed from entropy perturbations. There is no difference between halos formed in different ways. Both of them start to grow only at $t \sim t_{eq}$.

4.3.1 Final Mass

The total mass of the induced halo increases as more and more matter around the seed get separated from the Hubble flow and become virialized. The growth of the induced halo stops when the perturbations of dark matter start to evolve in a nonlinear way with growing mass os the induced halo, $M(t)$.

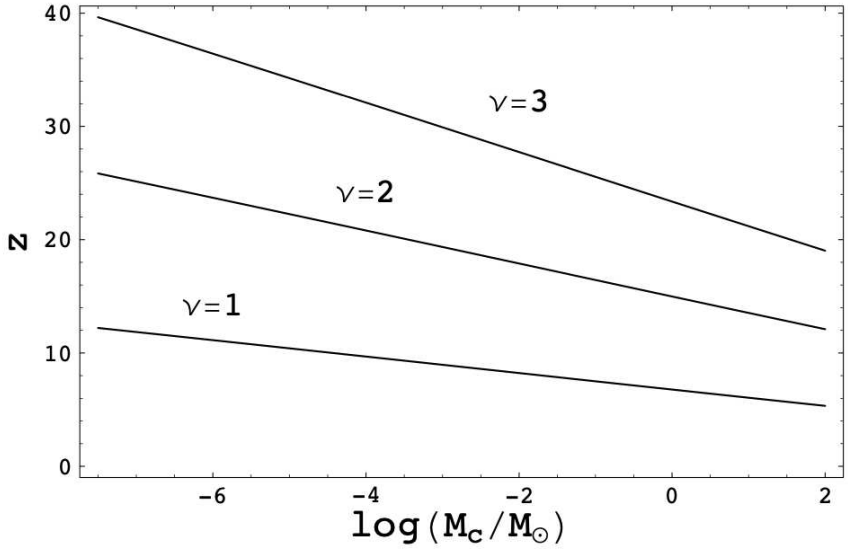

Figure 4.1: The redshift z of the growth termination for $\nu = 1, 2, 3$ fluctuations (from down to up), [4].

The growth of density contrast $\delta \propto t^{2/3}$ is the same in the matter domination epoch for the usual perturbations and perturbations accreting on a seed.

The condition for the growth stop of positive perturbations can be expressed as

$$\nu\sigma_{eq}(M) = \frac{9}{10}\frac{M_c}{M} \tag{4.40}$$

where ν is the value of density perturbation in terms of rms fluctuation $\sigma_{eq}(M)$. The right hand side of the Equation 4.40 is the amplitude of the fluctuations caused by the clump with mass M_c. Whereas the left hand side of the equation represents the Gaussian fluctuations at the time of equivalence, t_{eq}.

Large number of perturbations with positive $\nu \sim 1$, surrounding the ultradense dark matter halo results in the halo ceasing the growth in multiple directions and eventually destroys the secondary accretion. The negative perturbations $\nu < 0$ also dump the growth of the ultradense haloes due to the lower density of dark matter inside them.

Numerical solution to Equation 4.40 gives the final result of the mass of the induced dark matter halo, which is

$$M \sim (10^{1.5} - 10^{2.5})M_c \tag{4.41}$$

with $M_c \sim 10^{-8} - 10^2 M_\odot$.

The redshifts for different ν fluctuations at which the induced halo stops growing can be seen from the Figures 4.1. The corresponding final mass of the secondary accreted halo is illustrated in Figure 4.2 for different fluctuations $\nu = 1, 2, 3$.

4.4 Conclusion

The chapter has covered two types of dark matter halo formation. We have evaluated that in the matter dominated epoch the overdense region starts to collapse when the region is 5.55 times denser than the background (4.8). The collapsed region is not yet a fully formed dark matter halo, it has to undergo virialization process, as a result of which the overdense region becomes ~ 178 times denser than the background. The same

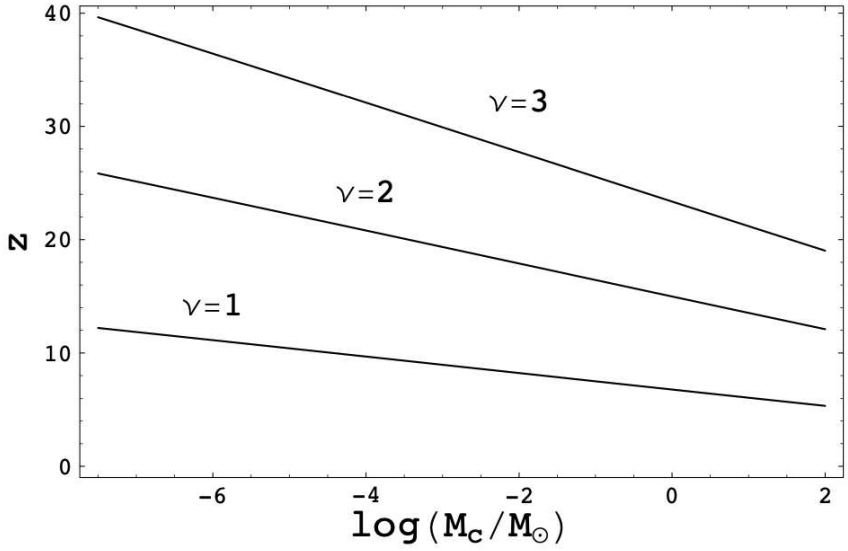

Figure 4.2: The final mass of the secondary accreted halo in relation to the seed mass M_c for $\nu = 1, 2, 3$ fluctuations, [4].

results can be derived using the linear perturbation approach described in the Section 4.2.2. The evolution of the overdensity of the region in the matter dominated epoch can be chracterized by (4.35).

Another way of dark matter halo formation is through secondary accretion onto a dark matter clump that was formed in the radiation dominated epoch. The secondary accretion begins with the matter domination, at the equivalence time. The matter will be accreting the initial seed until the growth stops, which can be evaluated by this criteria (4.40) [4].

Chapter 5

Properties of Dark Matter Halos

5.1 Introduction

This Chapter focuses on the properties of dark matter halos, namely the the core radius, the density profile and the structure of these objects. The core radius, density profile, and structure of ultradense dark matter halos are essential aspects of these cosmic structures, which play a pivotal role in the formation of galaxies and the large-scale structure of the Universe. The first section of this chapter (Sec. 5.2) investigates the effects on the maximum radius of the core of the dark matter clump, that was formed in the radiation dominated epoch. Section 5.3 describes one of the most commonly used density profiles, Navarro-Frenk-White (NFW) density profile. The authors of this model claim that this density profile is universal for all possible cosmological scenarios of dark matter halo formation. Section 5.4 extends the discussion on the NFW density profile by exploring its dependence on the characteristic overdensity. In this section, there is the derivation of this characteristic overdensity. Section 5.5 explores the mass density dependence of the halo. The results of this section are depicted in the plots that show the correlation between the mass and the density of the halo. From the previous section, it is known that the density profile is dependent on the overdensity. Another plot that is worth attention is the plot of concentration parameter with the mass of the halo. The concentration parameter (c), quantifies how concentrated the mass distribution is within a dark matter halo. It is typically defined as the ratio of the virial radius to the scale radius of the density profile. The scale radius is a characteristic radius that describes the inner region of the halo. Lastly, the section represents another plot of mass dependence and maximum circular velocity. The maximum circular velocity increases to the center of the halo until it reaches the maximum value. Section 5.6 introduces another density profile, Hernquist density profile, which scales as r^{-4}. The last Section 5.7 discussed the structure of the ultradense dark matter halos, which incorporates both abovementioned density profiles, NFW and Herquist. NFW densty profile is very accurate in the limits close to the halo's center, whereas the Hernquist density profile suits well to describe the outer regions formed by accretion.

5.2 Maximum Core Radius of Dark Matter Clumps

The region, $r < R_c$, inside the clump where the density stops growing is the core of that clump. According to some numerical simulation, the relative core takes values around $R_c/R \approx 10^{-2} - 10^{-3}$, where R is the radius of the virialized clump. What are the factors and underlying mechanism that affects on the core radius and hence of the central density of the clump?

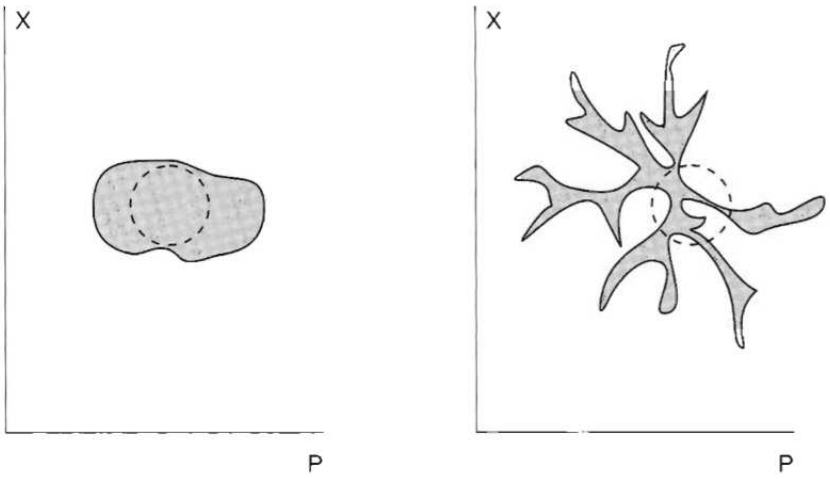

Figure 5.1: The left panel: in the beginning, particles occupy a certain region in the phase space. Right panel: the volume of this region doesn't change as the system evolves. However, the phase space density averaged over a macroscopic region (encircled) changes in the time and decreases in the dense regions of the phase space, [21].

5.2.1 Restrictions on the Core Radius

Louisville's theorem is one of the restricting factors that affects the core radius and puts boundaries on it. The Liouville's theorem is stated in the following way: the distribution function in the phase space in the collisionless system is constant in time, $f(p,q) = const$. This is valid at microscopic level. The Louisville's theorem is applicable only in the initial and final stages of the evolution of the system due to the intermediate entropy producing processes.

In reality, one is interested in the coarse grained phase space density, that is the phase space density averaged over macroscopic regions of phase space. In the beginning, the particles occupy a certain region of the phase space, but with time progress the underdense phase space volume becomes more occupied and the overdense volume of phase space gets diluted. This process is depicted in the Figure 5.1. Therefore, the coarse grained phase space density obeys the following inequality

$$f(\mathbf{k}, \mathbf{x}, t) \leq \max_k f_i(k) \tag{5.1}$$

The distribution function of the clump core can be expressed as

$$f_c = \frac{\rho_c}{v^3} \tag{5.2}$$

where ρ_c is the core density and v is the characteristic velocity in the core. We can restrict the core radius using the Louisville's theorem.

There are two sources of initial entropy: thermal velocities of dark matter particles at the decoupling and peculiar velocities in case of adiabatic perturbations. For the thermal part, the neutralino is a nonrelativistic nondegenarate at the moment of kinetic decoupling, t_d, hence it can be approximated with Maxwell's distribution function:

$$f_p(p) d^3r d^3p = \frac{\rho_m}{2(2\pi m k T)^{3/2}} e^{-\frac{p^2}{2mkT}} d^3r d^3p \tag{5.3}$$

where ρ_m is the dark matter density. It is expressed through the temperature using the entropy conservation condition $g_* T^3 a^3 = const$, g_* is the effective number of degrees of freedom at the temperature T, m is the dark matter particle mass.

The distribution function inside the core is less than the initial distribution function, so we can use the inequality:

$$f_c < f_p(p = 0) \tag{5.4}$$

For the isothermal density profile, $\rho(t) \propto r^{-2}$, the relative core radius is restricted as

$$\frac{R_c}{R} > \frac{2\pi^{1/2}\bar{\rho}^{1/4}T_d^{3/4}}{3^{1/4}G^{3/4}M^{1/2}m^{3/4}\rho_m^{1/2}(t_d)} \tag{5.5}$$

where T_d is the temperature of kinetic decoupling and is approximeted as $T_d \simeq 25$ MeV. The DM mass is taken to be $m = 100$ GeV. In [4] they used numerical methods to approximate the relative core radius and it is $R_c/R = 4 \times 10^{-3}$ for clump mass, $M/M_\odot = 10^{-6}$, average density, $\bar{\rho} = 3 \times 10^{-23}$, and density contrast, $\delta_{eq} = 0.009$.

The other entropy producing quantity is the peculiar velocity that is generated due to the gravitational instability. The peculiar velocity at some mass scale in the case of the flat metrics can be expressed as

$$\vec{v} = \frac{Ha}{4\pi}\Delta_x \int \frac{d^3x'\delta(\vec{x}')}{|\vec{x}' - \vec{x}|} \tag{5.6}$$

The calculations are analogous to the thermal velocity and for the peculiar velocity it takes the following form

$$\frac{R_c}{R} = 0.01\delta_{eq}^{9/2} \tag{5.7}$$

The numerical calculations from [4] give the result, $R_c/R = 6 \times 10^{-12}$ for the same parameters described before.

The other factor that restricts the central density and core radius is the annihilation of dark matter particles. The maximum density in the center of the clump is approxmated to be

$$\rho(r_{min}) \simeq \frac{m}{< \sigma v > (t_0 - t_f)} \tag{5.8}$$

where t_0 is the current moment of time and t_f is the moment of clump formation. Taking the isothermal density profile, $\rho(r) \propto r^{-2}$, the resulting relative core radius is

$$\frac{R_c}{R} \simeq \left(\frac{< \sigma v > t_0\bar{\rho}}{3m}\right)^{1/2} \tag{5.9}$$

Taking the thermal parameter value, $< \sigma v > \simeq 3 \times 10^{-26} cm^3 s^{-1}$ and the DM particle mass, $m = 100$ GeV, the other parameters as before, the relative core radius is $R_c/R = 2.6 \times 10^{-5}$.

In the real halos, there are mechanisms of regeneration of orbits with small angular momentum that go through the center of the clump, which make the central density larger than Eq. 5.8.

So, we can conclude that the most dominant factor that restricts the relative core radius is the Liouville restriction with the peculiar velocity out of all in the formation of the core in the clump formed at the matter-radiation equality.

The other process that could affect the core formation is the hierarchical clustering that gives rise to the entropy generation and hence dilutes the phase space density. Another process that makes a difference is the effect of the tidal forces which deflect particles from the center of the clump. However, the real mechanisms are yet unknown.

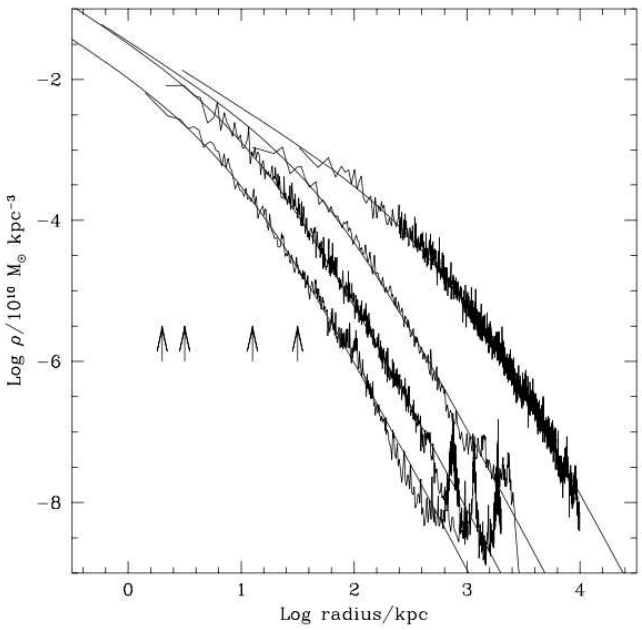

Figure 5.2: [29] The density profile of four halos spanning 4 orders of magnitude in mass, from $\sim 3 \times 10^{11} M_{\odot}$ to $\sim 3 \times 10^{15} M_{\odot}$. The arrows indicate the gravitational softening, h_g, of each simulation.

5.3 Navarro-Frenk-White Density Profile

In [29], the authors have run a high resolution N-body simulations to characterize the structure of cold dark matter (CDM) halos. They propose a universal density profile that can fit CDM halos of all masses by making an appropriate scaling. This profile is shallower than the isothermal one ($\rho(r) \propto r^{-2}$) near the center of a halo, and steeper than the isothermal in its outer regions. This density profile is called Navarro-Frenk-White (NFW), and is expressed as

$$\frac{\rho(r)}{\rho_{crit}} = \frac{\delta_c}{\frac{r}{r_s}\left(1 + \frac{r}{r_s}\right)^2} \tag{5.10}$$

where $r_s = 200/c$ is a characteristic radius, $\rho_{crit} = 3H^2/8\pi G$ is the critical density. r_{200} determines the mass of the halo, as

$$M_{200} = 200\rho_{crit}\frac{4\pi}{3}r_{200}^3 \tag{5.11}$$

and δ_c is the characteristic overdensity, c is the concentration and r_s is the scale radius. δ_c and c are related to each other through the following requirement

$$\delta_c = \frac{200}{3}\frac{c^3}{\left(\ln(1+c) - \frac{c}{1+c}\right)} \tag{5.12}$$

Figure 5.2 shows the density profiles of four halos of different masses plotted with respect to the radius of the halo. It is clear that the halos are denser in the core and the outer layers can go down in density in 6 orders of magnitude.

5.4 Characteristic Overdentsity

From the NFW density profile we see that it is dependent on the characteristic overdensity, δ_c. In [30] authors give a step by step procedure to calculate this quantity for Einstein

de Sitter characterized by $\Omega_0 = 1, \Lambda = 0$, open ($\Omega_0 < 1, \Lambda = 0$) and flat ($\Omega_0 + \Lambda = 1$) universes.

We can characterize a halo of mass M with its virial radius and circular velocity,

$$r_{200} = 1.63 \times 10^{-2} \left(\frac{M}{h^{-1} M_\odot} \right)^{1/3} \left(\frac{\Omega_0}{\Omega(z_0)} \right)^{-1/3} (1 + z_0)^{-1} h^{-1} kpc \tag{5.13}$$

$$V_{200} = \left(\frac{GM}{r_{200}} \right)^{1/2} = \left(\frac{r_{200}}{h^{-1} kpc} \right) \left(\frac{\Omega_0}{\Omega(z_0)} \right)^{1/2} (1 + z_0)^{3/2} km/s \tag{5.14}$$

And the density profile can be expressed as

$$\rho(r) = \frac{3H_0^2}{8\pi G} (1 + z_0)^3 \frac{\Omega_0}{\Omega(z_0)} \frac{\delta_c}{cx(1 + cx)^2} \tag{5.15}$$

where $x = \frac{r}{r_{200}}$ and c is the concentration parameter. As you can see, the density profile can be fully defined either through the characteristic overdensity, δ_c, or the concentration parameter, c.

The corresponding circular velocity, $V_c(r)$, is

$$\left(\frac{V_c(r)}{V_{200}} \right)^2 = \frac{1}{x} \frac{\ln(1 + cx) - \frac{cx}{1+cx}}{\ln(1 + c) - \frac{c}{1+c}} \tag{5.16}$$

The characteristic overdensity can be determined by the collapse redshift, z_{coll}. The collapse redshift, $z_{coll}(M, f)$, can be defined as the time at which half of the mass of the halo was first contained in progenitors more massive than some fraction of the final mass and can be computed using the following equation

$$\mathrm{erfc}\left(\frac{\delta_{crit}(z_{coll}) - \delta^0_{crit}}{\sqrt{2(\Delta_0^2(fM) - \Delta_0^2(M))}} \right) = \frac{1}{2} \tag{5.17}$$

where $\Delta_0^2(M)$ is the linear variance of the power spectrum at $z = 0$ smoothed with a top-hat filter of mass M, $\delta_{crit}(z)$ is the density threshold for spherical collapse by redshift z, and $\delta^0_{crit} = \delta_{crit}(0)$.

Assuming the characteristic overdensity of a halo to be proportional to the density of the universe at the corresponding z_{coll} then implies

$$\delta_c(M|f) = C\Omega_0 (1 + z_{coll}(M, f))^3 \tag{5.18}$$

where C is a proportionality constant which might depend on f and the power spectrum.

Now the equation for the characteristic overdensity becomes

$$\frac{\delta_{crit}(z_{coll})}{\delta_{crit}(z_0)} = \frac{\delta^0_{crit}(\Omega(z_{coll}, \Lambda))}{\delta^0_{crit}(\Omega(z_0, \Lambda))} \frac{D(z_0, \Omega_0, \Lambda)}{D(z_{coll}, \Omega_0, \Lambda)} = 1 + \frac{0.477}{\delta_{crit}(z_0)} \sqrt{2(\Delta_0^2(fM) - \Delta_0^2(M))} \tag{5.19}$$

where $D(z, \Omega_0, \Lambda)$ is defined as

$$D(z, \Omega_0, \Lambda) = \begin{cases} 1/(1 + z), & \text{if } \Omega_0 = 1 \text{ and } \Lambda = 0, \\ F_1(w)/F_1(w_0), & \text{if } \Omega_0 < 1 \text{ and } \Lambda = 0, \\ F_2(y)F_3(y)/F_2(y_0)F_3(y_0), & \text{if } \Omega_0 + \Lambda = 1, \end{cases} \tag{5.20}$$

where we used auxiliary functions and defined them as follows

$$w_0 = \frac{1}{\Omega_0} - 1 \tag{5.21}$$

$$w = \frac{w_0}{1+z} \tag{5.22}$$

$$F_1(u) = 1 + \frac{3}{u} + \frac{3(1+u)^{1/2}}{u^{3/2}} \ln\left[(1+u)^{1/2} - u^{1/2}\right] \tag{5.23}$$

$$y_0 = (2w_0)^1/3 \tag{5.24}$$

$$y = \frac{y_0}{1+z} \tag{5.25}$$

$$F_2(u) = \frac{(u^3+2)^{1/2}}{u^{3/2}} \tag{5.26}$$

$$F_3(u) = \int_0^u \left(\frac{u'}{u'^3+2}\right)^{3/2} du' \tag{5.27}$$

A numerical approximation to the Ω-dependence of the critical threshold for the spherical collapse can be expressed as

$$\delta^0_{crit}(\Omega,\Lambda) = \begin{cases} 0.15(12\pi)^{2/3}, & \text{if } \Omega_0 = 1 \text{ and } \Lambda = 0, \\ 0.15(12\pi)^{2/3}\Omega^{0.0185}, & \text{if } \Omega_0 < 1 \text{ and } \Lambda = 0, \\ 0.15(12\pi)^{2/3}\Omega^{0.0055}, & \text{if } \Omega_0 + \Lambda = 1, \end{cases} \tag{5.28}$$

which can be used to compute

$$\delta_{crit}(z_0) = \frac{\delta^0_{crit}(\Omega(z_0))}{D(z_0,\Omega_0,\Lambda)} \tag{5.29}$$

Now we have to compute the variance of the power spectrum on mass scale M, extrapolated linear;y to $z = 0$, $\Delta^2_0(M)$. For the power law power spectrum, $P(k) \propto k^n$, we get

$$\Delta^2_0(M) = \delta^0_{crit}\left(\frac{M}{M_*(z=0)}\right)^{-(n+3)/6} \tag{5.30}$$

where we have normalized the spectrum by $M_*(z = 0)$ which is the present nonlinear mass. A CDM spectrum is usually normalized by σ_8, which is the rms fluctuations within a sphere of radius $8h^{-1}$ Mpc and its variance can be expressed as

$$\Delta_0(M) = \frac{\sigma_8 F_4(M_8)}{F_4(M_h)} \tag{5.31}$$

where

$$M_8 = 6.005 \times 10^{14}(h\Omega_0)^3 \tag{5.32}$$

$$M_h = \left(\frac{M}{h^{-1}M_\odot} h^3\Omega_0^2\right) \tag{5.33}$$

$$F_4(u) = A_1 u^{0.67}[1 + (A_2 u^{-0.1} + A_3 u^{-063})^p]^{1/p} \tag{5.34}$$

with $A_1 = 8.6594 \times 10^{-12}$, $A_2 = 3.5$, $A_3 = 1.628 \times 10^9$ and $p = 0.255$.

The Equations 5.20-5.34 can solve the Eq.5.19 and find the collapse redshift for a halo of mass M. In the calculation it is preferred to use $f = 0.01$. The reason for this choice will be discussed later. Once the collapse redshift is found we can express the characteristic overdensity

$$\delta_c(M,f) \sim 3 \times 10^3 \Omega(z_0)\left(\frac{1+z_{coll}}{1+z_0}\right)^3 \tag{5.35}$$

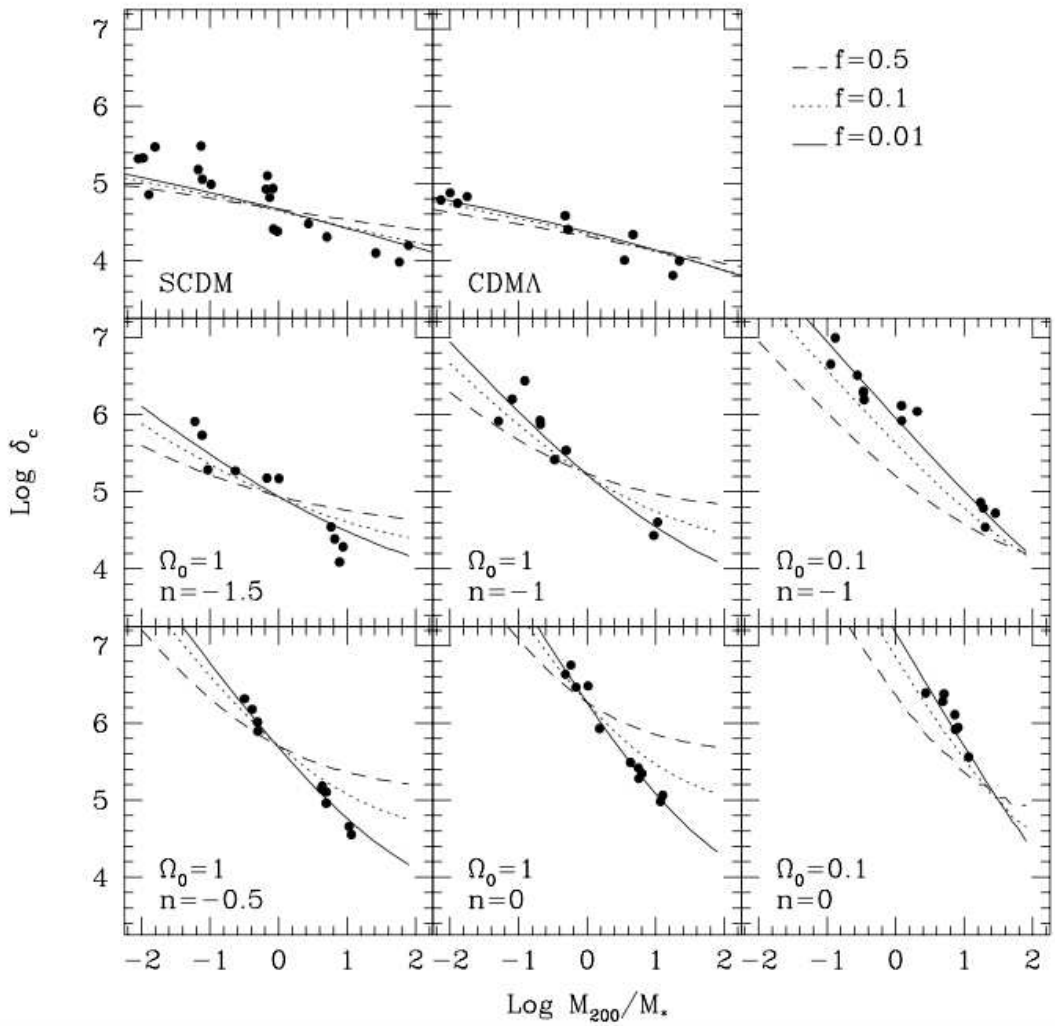

Figure 5.3: [30] The correlation between the mass of a halo and its characteristic overdensity. Masses are given in units of the nonlinear mass scale, M_*. Overdensities are relative to the critical value. There are three curves for each value of f, mass fraction.

5.5 The Mass Dependence of Halo Structure

The mass and density dependence of halo can be illustrated in Figure 5.3. The characteristic overdensity of a halo increases for lower masses. This result supports the idea that less massive systems have higher redshift collapse, meaning that they collapse earlier in the history of the universe. This model assigns to each halo of mass M a collapse redshift, z_{coll}, defined earlier.

Similar figure, illustrating the mass and density dependence is Figure 5.4, which is different in the fact that it is the concentration parameter plotted to the mass. The concentration parameter is defined as $c = r_{200}/r_s$.

To support the argument of the mass dependence with the collapse redshift, we have to take $f \ll 1$ to give a good fit to the data. In this limit, $\Delta_0^2(fM) >> \Delta_0^2(M)$, which results in

$$\delta_{crit}(z_{coll}) = \delta^0_{crit} + C'\Delta_0(fM) \tag{5.36}$$

where $C' \approx 0.7$. For $f \ll 1$, $\delta_{crit}(z_{coll}) \gg \delta^0_{crit}$ for all masses in the range defined in the simulations. Since $M_*(z_{coll})$ is defined as $\Delta_0(M_*(z_{coll})) = \delta_{crit}(z_{coll})$, it means that the

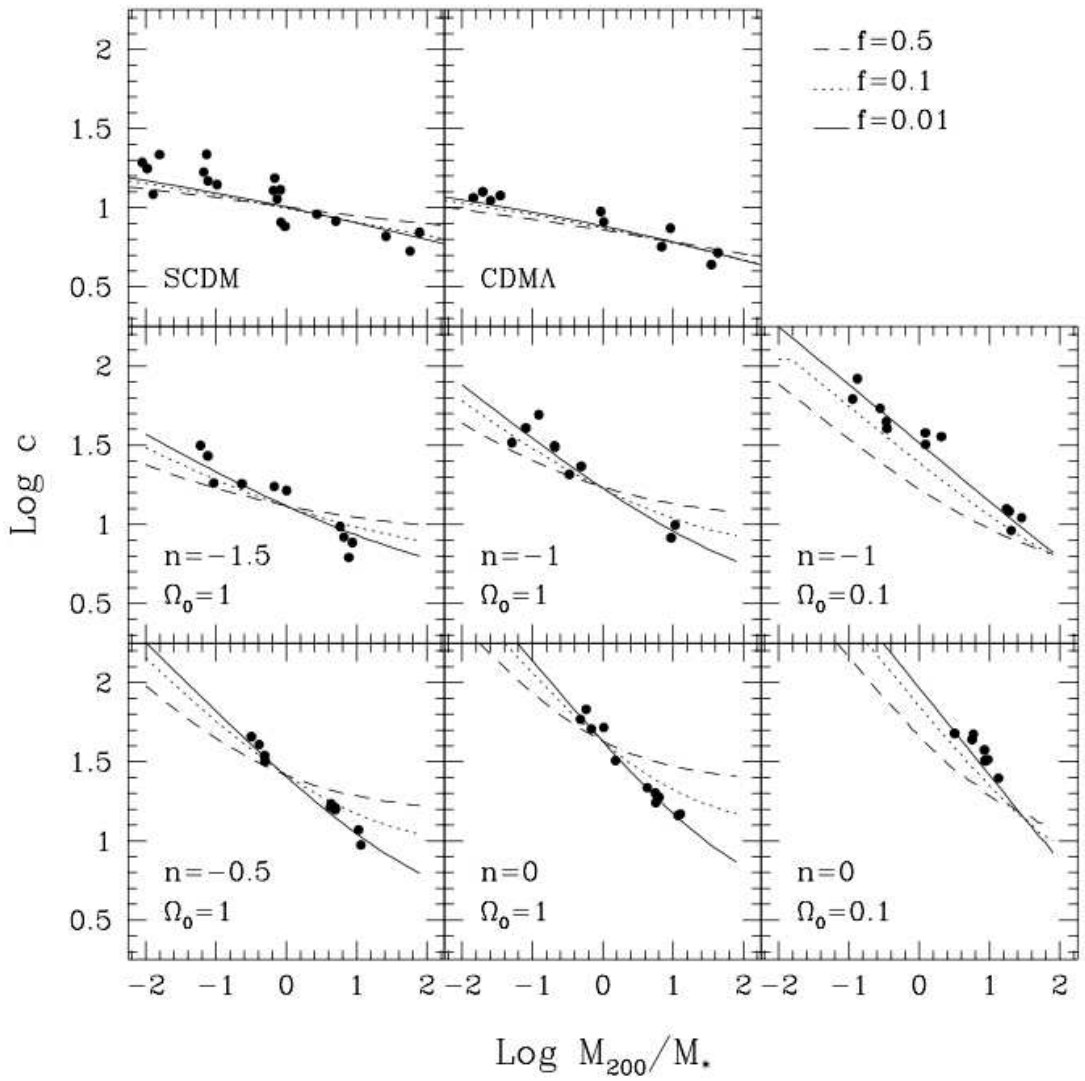

Figure 5.4: [30]The correlation between the mass of a halo and its concentration parameter. Masses are given in units of the nonlinear mass scale, M_*. Overdensities are relative to the critical value. There are three curves for each value of f, mass fraction.

characteristic overdensity of a halo is proportional to the mean density of the Universe at the time when $M_* \approx fM$. In other words, when the characteristic nonlinear mass is a fixed small fraction of the final mass of the halo, the characteristic overdensity of the halo is proportional to the mean density of the universe. This implies that $\delta_c \propto M^{-(n+3)/2}$.

So, the reason we prefer smaller values of f is that the data taken from the Eq.5.36 that proves the mass-density dependence correlates better with the Einstein de-Sitter simulations. Another interesting dependence is that the characteristic overdensity decrease for more negative values of the spectral index, n. Meaning that the characteristic density of a halo of mass M_* depends on the shape of the power spectrum on scales $\sim fM_*$.

There is a maximum characteristic speed for each halo, V_{max}. From the Figure 5.5, we can clearly see its strong correlation with the mass of the halo. The circular velocity rise to the center of the halo and reach the maximum value at $x_{max} \sim 2/c$, where $x = r/r_{200}$ and c is the concentration parameter. More centrally concentrated halos, with higher characteristic overdensity and concentration parameter, have higher values of V_{max}/V_{200}. As a result, $M_{200} - V_{max}$ is almost the same as the $M_{200} - V_{200}$, which suggests for strong correlation between mass and the characteristic velocity. This tight correlation between mass and velocity is called Tully-Fisher relation.

As a result, Figures 5.3-5.5 supports the conclusion that the characteristic overdensity of a halo is dependent on the mean matter density of the universe at the time of collapse. Overdensities of halos of mass M_* increase with the spectral index, but for higher masses, $M \gtrsim 10M_*$, the differences between models is negligible. Also, there is a strong dependence of the density profile of a halo on the density parameter Ω_0.

5.6 Hernquist Density Profile

The Hernquist density profile is a mathematical model used to describe the density distribution of matter in spherically symmetric systems, such as dark matter halos or galaxies. It was introduced by Lars Hernquist in 1990 and is commonly used in astrophysical simulations to represent the density profiles of stellar systems and dark matter haloes. The Hernquist profile is particularly useful for describing the density distribution of galaxies and galactic bulges.

The density profile [23],

$$\rho(r) = \frac{M}{2\pi}\frac{a}{r}\frac{1}{(r+a)^3} \tag{5.37}$$

where M is the total mass of the object and a is the scale length. Note that the density profile scales like $\rho \propto r^{-4}$.

5.7 Structures of Ultradense Dark Matter Halos

The characteristic density of dark matter halo, ρ_h, depends on the mean density of the universe at the time of halo formation as it was pointed out in the Section 5.4. According to [17], [16], it is a general consequence of mass accretion process in the cosmological context. Therefore, the halos formed at the radiation domination epoch, the characteristic density can be expressed as

$$\rho_h = \alpha \rho_{r,0} a_f^{-4} \tag{5.38}$$

where $\rho_{r,0}$ is the radiation density today, α is a proportionality factor, a_f is the expansion rate at the time of the halo formation.

The ultradense dark matter halos should form with NFW density profile, characterized by scale radius, r_h and scale density, ρ_h. The halo's outer virial radius is taken to be

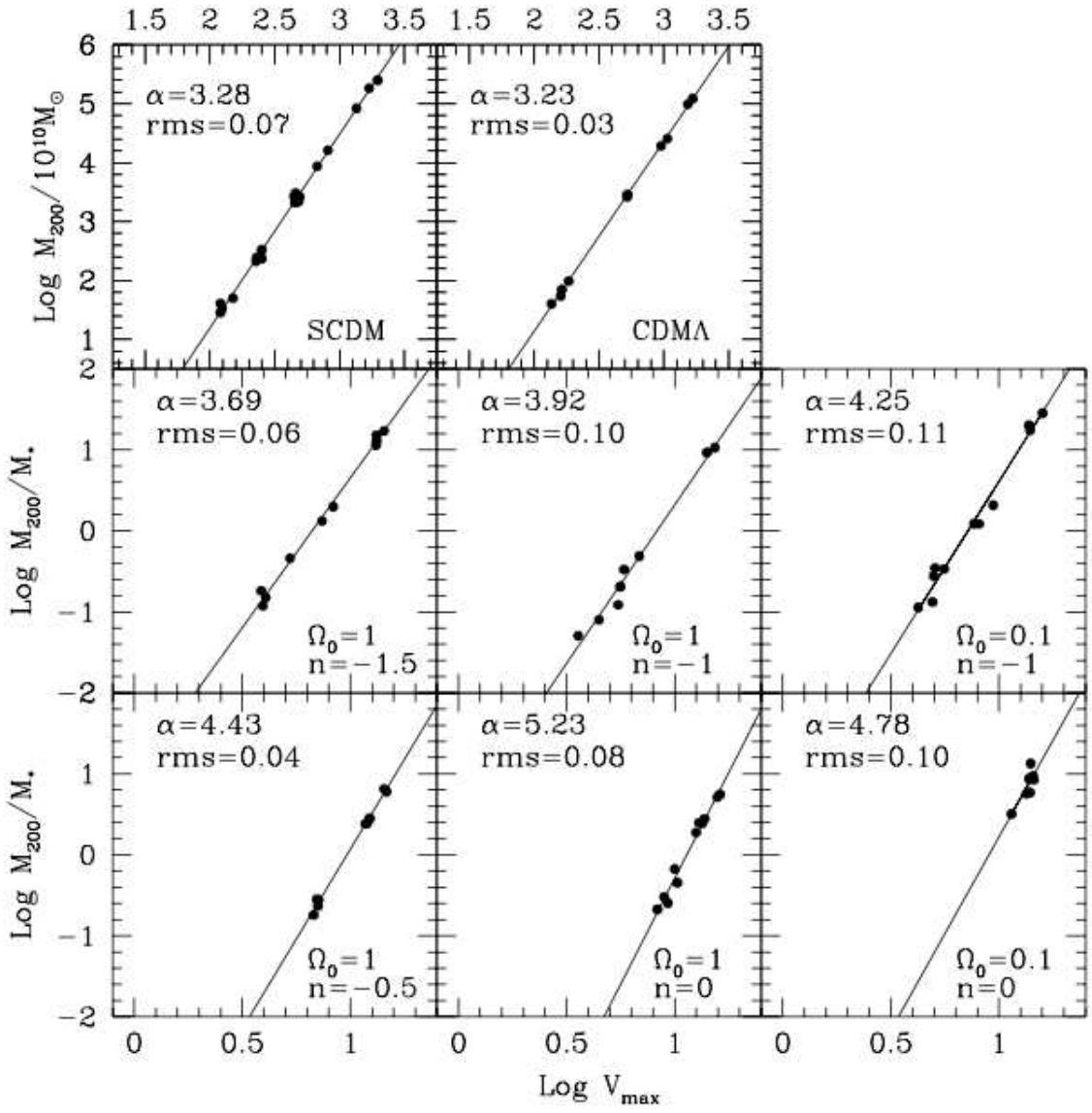

Figure 5.5: [30] The mass dependence of the maximum circular velocity of a halo. The mass is given in the units of $10^{10} M_{\odot}$. Velocity units are arbitrary in the power law panels. Power law fits are of the form $M \propto V_{max}^{\alpha}$.

$R_{vir} = 2r_h$ and integrating the NFW density profile up to R_{vir}, we obtain the mass of the halo at the time of its formation

$$M \simeq 5.4\rho_h r_h^3 \tag{5.39}$$

We can describe the mass M as the mass of the densest central part of the halo. Since further acquisition of mass will be through accretion.

The NFW density profile is accurate in the limit near halo's center, up to the scale radius, r_h. However, it is not accurate at the distance much larger than r_h. The density profile beyond that limit is set long after the halo formation by the halo's accretion history. The density profile predicted in this case is of the form $\rho \propto r^{-4}$. Due to these considerations, the late time density profile of an ultradense halo with Hernquist form according to [14] looks as

$$\rho(r) = \rho_h \left(\frac{r}{r_h}\right)^{-1} \left(1 + 0.58\frac{r}{r_h}\right)^{-3} \tag{5.40}$$

where the numerical factors were tuned such that the density profile matches the NFW profile up to a few r_h and for r much larger, the density profile scales as $\rho \propto r^{-4}$. The upper panel in Figure 5.6 shows the plot of this density profile with respect to the radial distance, r. The mass of the halo is taken to be $M = 1.9 \times 10^{-6} M_\odot$ and the characteristic radius $r_h = 1100\alpha^{-1/3} R_\odot$. Integrating this density profile gives $3.5M$, where M is the mass of the halo at its formation (5.39).

The central structure of the collisionless dark matter halos remain almost the same throughout the evolution and the characteristic density and radius remain accurate even today. One possibility in which it could be wrong is the merger of halos. Simulations suggest that the merger remnant's characteristic density is not lower than that of the progenitors. Thus the mergers just shift the mass of dark matter halos to higher values.

Ultradense dark matter halos accrete onto larger halos at later times. The extreme high density of the ultradense halos allow them to avoid any impact from the tidal forces of the larger halo. The middle panel of the Fig.5.6 illustrates $v_{circ}/r = \sqrt{F/r}$ (blue line) with respect to the radial distance from the halo's center. v_{circ} is the circular orbit velocity and F is the halo's central force. If we compare this quantity to the $\sqrt{dF_{MW}/dR}$ (red line), we realize that the impact of the Galactic tidal forces are only feasible at distances larger than $10^6 R_\odot$ from the halo's center. This allows us to neglect the tidal forces of the galaxy.

However, encounters with individual stars may impact the halo more significantly. The shocks by stellar encounters become important for the ultradense halo's density profile only beyond $10^4 - 10^5 R_\odot$. It is unclear how exactly they impact the density profile that scales as $\rho \propto r^{-4}$, since it is considered that this scaling includes the effect from these encounters.

The last panel of the Figure5.6 shows the deflection of light under the influence of the ultradense dark matter halos characterized by M and r_h specified earlier. The deflection angle is

$$\frac{4G}{c^2}\frac{M_{2D}(r)}{r} \tag{5.41}$$

where M_{2D} is

$$M_{2D}(r) \equiv \int_0^r 2\pi b db \int_{-\infty}^{+\infty} dz \rho(\sqrt{b^2 + z^2}) \tag{5.42}$$

which is the mass within an infinite cylinder of radius r.

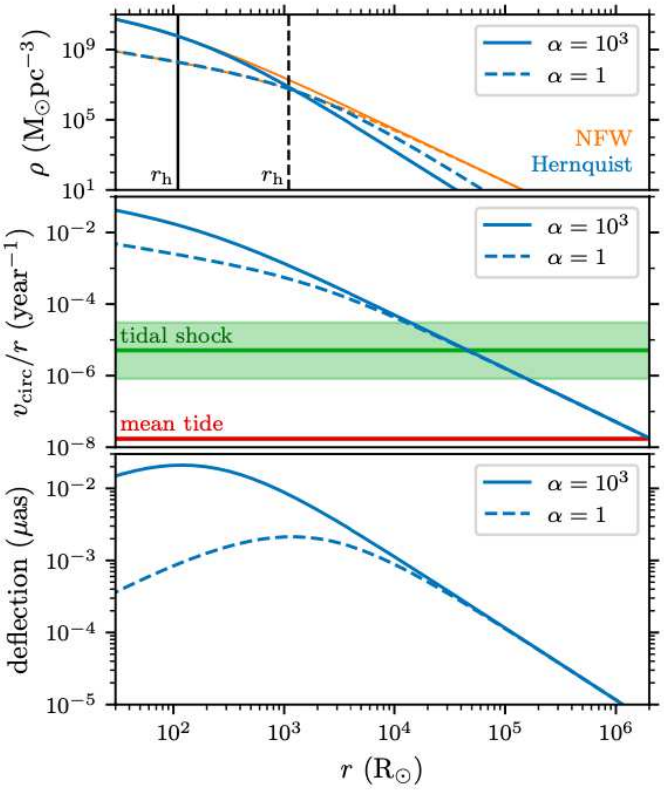

Figure 5.6: The properties of an ultradense dark matter halo with mass at the moment of formation being $M = 1.9 \times 10^{-6} M_\odot$ and the characteristic radius $r_h = 1100\alpha^{-1/3} R_\odot$. Upper panel shows the density profile with respect to the radial distance from the center of the halo. The middle panel shows the behavior of v_{circ}/r with respect to the radial distance from the center of the halo compared to the tidal forces of the Milky Way galaxy and the shocks produced by encounters with individual stars within a galaxy. The lower panel shows the deflection of the light under the influence of the halo, [14].

5.8 Conclusion

In conclusion, the exact mechanism for the core formation of the ultradense dark matter halo is yet unknown. There are certain factors that affect the growth of the core. One of the dominant factors to affect the core formation and eventually its maximum size is the peculiar velocity. Other factors are hierarchical clustering, tidal effects and DM annihilation [4]. To find out more about the exact mechanisms of the core formation, it is necessary to run numerical simulations of the ultradense dark matter halos formation in the radiation dominated epoch, taking into account the above mentioned factors and the cosmological scenario.

Sections 5.4, 5.5 presents plots that contain significant outcomes about the characteristic overdensity. The conclusion to draw from these plots is that the overdensity depends on the mean density of the universe at the time of collapse [30]. The density profiles of the dark matter halo depends on the overdensity (5.12). Finally, the structure of the dark matter halo is summarized in the last section, which incorporated NFW (5.12) and Hernquist (5.37) density profiles to describe the structure of the ultradense dark matter halos [15].

Chapter 6

Statistical Abundance of Dark Matter Halos

6.1 Introduction

The statistical abundance of dark matter halos refers to the distribution of dark matter halos in the Universe as a function of their mass or size. This statistical abundance is a crucial concept in cosmology and large-scale structure studies, as it helps us understand how common or rare dark matter halos of different sizes are in the cosmic landscape. Several key aspects of the statistical abundance of dark matter halos are mass function, power spectrum, halo bias, observational probes, redshift evolution, cosmological probes. This chapter is focused more on the mass function and power spectrum. The fisrt Section (6.2) introduces the Press-Schetcher formalism that is a fundamental tool for understanding the distribution and abundance of dark matter halos, serving as a basis for more sophisticated models and simulations in modern cosmology. Section 6.3 introduces a more refined version of the Press-Schechter formalism, Excursion Set formalism, which takes into account nonlinear evolution of the dark matter halos, whereas the Press-Schechter formalism is based on the spherical collapse model. Section 6.4 considers ellipsoidal collapse of the overdense region resulting in a dark matter halo formation and investigates its abundance in terms of considering the mass function and the power spectrum of this fluctuation. Finally, Section 6.5 discusses the formation of the primordial black holes (PBH) and dark matter halos and their power spectrum.

6.2 Press-Schechter Formalism

The Press-Schechter formalism is based on the assumption that the growth of cosmic structures, such as dark matter haloes, occurs through the gravitational collapse of small density perturbations in the early Universe. The Press-Schechter formalism provides a simple analytical approximation for the abundance of dark matter halos in the early Universe. It has been a useful tool in cosmology for understanding the general behavior of halo distributions and making predictions about the large-scale structure of the Universe. However, it has some limitations, and more refined methods, such as extended Press-Schechter and excursion set formalisms, have been developed to improve the accuracy of predicting halo abundances and their properties in numerical simulations.

The distribution and abundance of dark matter halos in the matter-dominated epoch can be characterized by the halo mass function. The halo mass function describes the statistical distribution of halo masses, indicating the number density of halos as a func-

tion of their mass. It provides insights into the growth and evolution of structures in the Universe. The Press-Schechter mass function is a fundamental theoretical result in cosmology that provides an approximate statistical distribution of dark matter halos as a function of their mass. The mass function gives the comoving number density of dark matter halos per unit mass interval, and it is expressed as, [34]

$$\frac{dn}{d\log M} = \frac{\rho_m}{M}\frac{d}{d\log M}\text{erfc}\left(\frac{\nu}{\sqrt{2}}\right) \tag{6.1}$$

where $\nu \equiv \delta_c/\sigma(M)$, δ_c is the overdensity threshold for the collapse to take place, in the matter dominated universe is usually $\delta_c = 1.686$.

The Press-Schechter mass function was one of the first attempts to predict the abundance and distribution of dark matter haloes in the Universe based on the primordial density fluctuations. While it provides a simple and useful analytical approximation, it has some limitations and discrepancies compared to results from large-scale numerical simulations.

6.3 Excursion Set Mass Function

The excursion set formalism provides a more accurate and refined description of the abundance and properties of dark matter halos compared to the original Press-Schechter formalism. It takes into account the non-linear evolution of density fluctuations and includes higher-order corrections, leading to improved agreement with results from large-scale numerical simulations.

The excursion set mass function is, [7]

$$\frac{df}{d\log M} = \sqrt{\frac{2}{\pi}}\frac{(\nu + 0.556)e^{-\frac{1}{2}(\nu+1.34)^2}}{(1+0.0225\nu^{-2})^{0.15}}\left|\frac{d\log\sigma_M}{d\log M}\right| \tag{6.2}$$

where f is the dark matter mass fraction in collapsed region of mass M, $\nu \equiv 3/\sigma_M$ and the rms density contrast, σ_M is

$$\sigma_M^2 = \int_0^\infty \frac{dk}{k}P(k)W^2(kr) \tag{6.3}$$

where $W(x) \equiv 3(\sin x - x\cos x)/x^3$, $M = \frac{4\pi}{3}\rho_{m,0}r^3$, $\rho_{m,0}$ is the comoving dark matter density. The upper panel of Figure 6.1 illustrates $df/d\log M$ for collapsed regions of mass M.

For the dark matter halo formation to take place the local region has to be matter dominated, the corresponding formation scale factor can be expressed as and is illustrated in the upper middle panel of Figure 6.1

$$a_f(M) \sim e^2\left|\frac{r\int_0^\infty dkP(k)W'(kr)}{\int_0^\infty \frac{dk}{k}P(k)W(kr)}\right|a_{eq} \tag{6.4}$$

The power spectrum for this calculation is

$$P(k,a) = I_1^2\left(\log\left(\sqrt{2}I_2\frac{k}{k_{eq}}\frac{a}{a_{eq}}\right)\right)^2 P_\zeta(k) \tag{6.5}$$

where $I_1 \simeq 6.4$, $I_2 \simeq 0.47$ from [1]. The ellipticity of the initial tidal field for a region of mass M at its collapse time is

$$e(M) = \frac{1}{3}\left(1 - \left(1 + \frac{\sigma_M}{\sqrt{5}}\right)^{-1}\right) \tag{6.6}$$

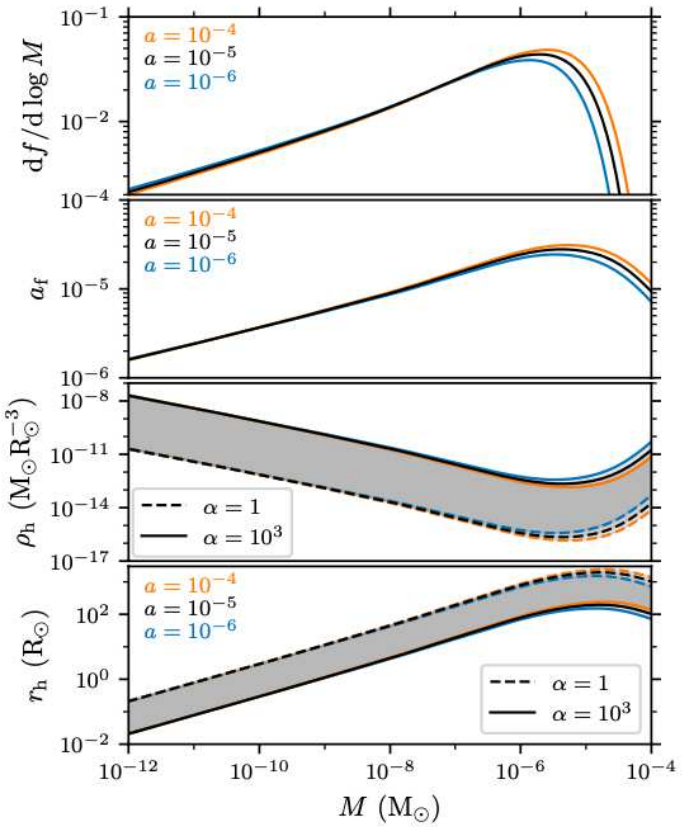

Figure 6.1: Ultradense halos arising from the primordial power spectrum expressed in (6.5). The upper panel shows the differential dark matter mass fraction for the collapsed region of mass M. The upper middle panel shows the scale factor at the time of collapse of the region of mass M. The lower middle panel shows the characteristic density of the halo. The lower panel shows the characteristic radius of the halo, [14].

6.4 Ultradense Dark Matter Halo's Structure

Consider the ellipsoidal collapse of overdense region that leads to ultradense dark matter halo formation. The most probable values for e and p to describe the initial tidal field as discussed in the section above are

$$e = (\sqrt{5}\delta_c/\sigma) \qquad\qquad p = 0 \tag{6.7}$$

Inserting them into the critical collapse threshold, $\delta_c = 3/(1-3e+p)$, we can express it in terms of rms density contrast, σ

$$\delta_c = 3\left(1 + \frac{\sigma}{\sqrt{5}}\right) \tag{6.8}$$

In the excursion set formalism this threshold corresponds to the moving barrier, [7]

$$B(S) \equiv 3\left(1 + \sqrt{\frac{S}{5}}\right) \tag{6.9}$$

with $S \equiv \sigma^2$. For a Gaussian random walk, the distribution of first barrier crossings in this scenario is well approximated by

$$F(S) = \frac{3 + 0.556\sqrt{S}}{\sqrt{2\pi S^3}} \exp\left(-\frac{B(S)^2}{2S}\right)\left(1 + \frac{S}{400}\right)^{-0.15} \tag{6.10}$$

This distribution results in the following Press-Schechter mass function for the halo

$$\frac{dn}{d\log M} = \sqrt{\frac{2}{\pi}}\frac{(\nu + 0.556)e^{-\frac{1}{2}(\nu+1.34)^2}}{(1 + 0.0225\nu^{-2})^{0.15}}\frac{d\log\nu}{d\log M}\frac{\rho_{m,0}}{M} \tag{6.11}$$

where $\rho_{m,0} \simeq 33 M_\odot \mathrm{kpc}^{-3}$ is the comoving dark matter density and $\nu \equiv 3/\sigma_M$. Here, σ_M is the rms density contrast smoothed on the mass scale, M, which we evaluate using a sharp-k filter in order to accommodate power spectra that deviate significantly from scale invariance.

$$\sigma_M^2 = \int_0^{k_M} \frac{dk}{k}\mathcal{P}(k,a) \tag{6.12}$$

with $M \equiv 6\pi^2\rho_{m,0}k_M^{-3}$, which implies

$$\frac{d\log\nu}{d\log M} = \frac{\mathcal{P}(k_M,a)}{6\sigma_M^2} \tag{6.13}$$

And,

$$\mathcal{P}(k,a) \equiv \frac{k^3}{(2\pi)^2}P(k,a) \tag{6.14}$$

which is the dimensionless matter power spectrum, which is a function of time. And, the power spectrum of the primordial curvature perturbations

$$\mathcal{P}(k,a) = I_1^2\left(\log\left(\sqrt{2}I_2\frac{k}{k_{eq}}\frac{a}{a_{eq}}\right)\right)^2\mathcal{P}_\zeta(k) \tag{6.15}$$

where $\mathcal{P}_\zeta$ is the dimensionless power spectrum of primordial curvature perturbations.

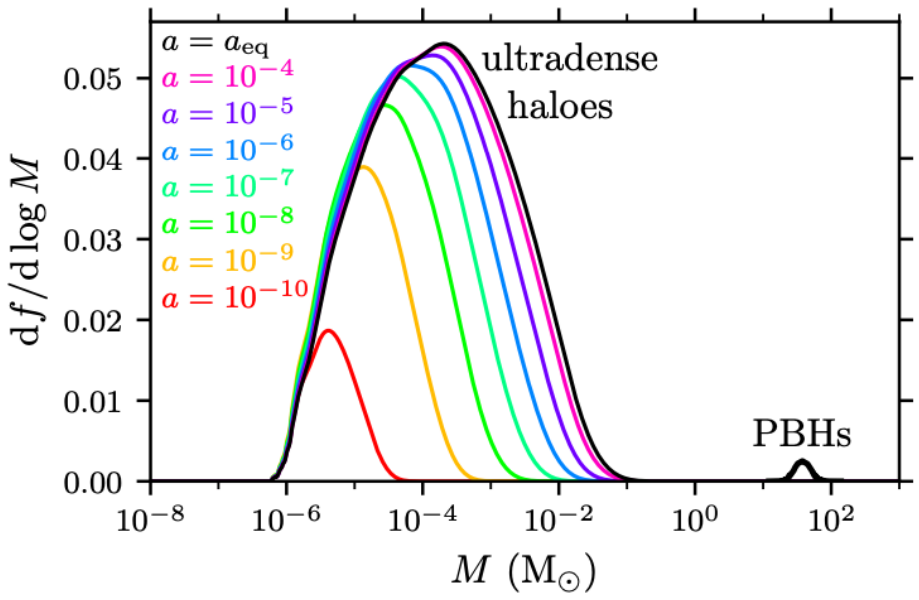

Figure 6.2: Differential dark matter mass fraction in ultradense halos and PBHs in the double inflation scenario, [15].

6.5 Ultradense halos and Primordial Black Holes

Typical density peak that results in a collapse to produce a halo requires $\zeta \gtrsim 0.15$, whereas for a PBH, this requirement is around unity. Due to this argument, ultradense minihalos are expected to outnumber PBHs in scenarios where there is nonrelativistic dakr matter decoupled from the radiation at the time that the large amplitude initial density variations are entering the horizon. There are two possibilities, first - PBHs are only a fraction of dark matter and ultradense halos form from dark matter particles, second - PBHs are all of dark matter but have a mass function that extends over many rders of magnitude, so that the ultradense halos are clusters of much smaller PBHs.

Consider the scenario [24], when a double inflation model yields a complicated primordial power spectrum that produces asteroid-mass PBHs that comprise almost all of the dark matter while also producing a small abundance of 10 to $100 M_\odot$ PBHs to explain binary coaslescence detections. Then we expect that the density fluctuations that produce more massive PBHs also create ultradense halos that consist of asteroid-mass PBHs. Figure 6.2 shows the differential mass fraction in ulradense halos that form during radiation dominated epoch, from which we can see that the massive PBHs comprise only 0.2 per cent of the dark matter. Whereas dark matter halos coming from the same density variations comprise about 40 per cent of the dark matter mass.

Another scenario [9], where the primordial power spectrum is

$$\mathcal{P}_\zeta(k) = \begin{cases} A_s \left(\frac{k}{0.05 \mathrm{Mpc}^{-1}} \right)^{n_s - 1}, & \text{if } k < k_1 \\ A_1 \left(\frac{k}{10^6 \mathrm{Mpc}^{-1}} \right)^{n_s - 1}, & \text{if } k > k_1 \end{cases} \tag{6.16}$$

where $A_s = 2.1 \times 10^{-9}$ and $n_s = 0.96$ to match the data from the cosmic microwave background, the power is boosted to $A_1 \simeq 0.022$ at small scales $k > k_1 \simeq 190 \mathrm{Mpc}^{-1}$ in order to produce PBHs in the right abundance to comprise all of the dark matter. This spectrum is featureless and nearly scale invariant for $k > k_1$, but it yields the nontrivial PBH mass function that is depicted in Figure 6.3.

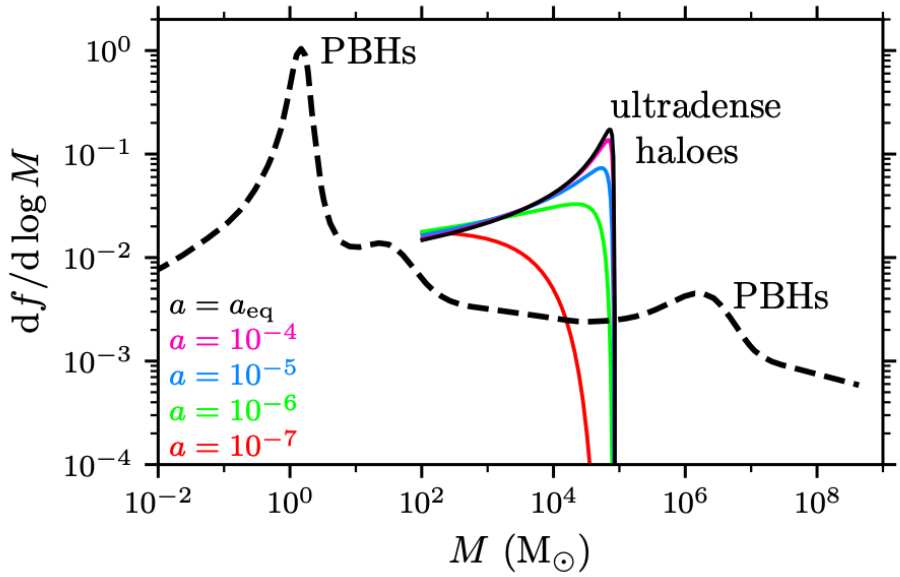

Figure 6.3: Differential dark matter mass fraction in ultradense halos and PBHs in the PBH scenario, [15].

In this second scenario, the bulk of dark matter consists of $O(1)M_\odot$ PBHs, but a tail of much larger PBHs act as seeds for the supermassive black holes found at the centers of galaxies. The density variations on scales large enough to produce such PBHs also cause the solar mass PBHs to cluster in ultradense halos up to nearly $10^5 M_\odot$. Whereas PBHs larger than $10^3 M_\odot$ comprise only 3 per cent of the dark matter, 30 per cent of the dark matter resides in ultradense halos above this mass scale. If halos of mass M_{halo} and PBHs of mass M_{PBH} form from density fluctuations of the same scale, then

$$M_{halo} \sim M_{PBH}^{3/2} M_{eq}^{-1/2} \tag{6.17}$$

approximately relates two mass scales, where $M_{eq} \simeq 3 \times 10^{17} M_\odot$ is the horizon mass at the matter-radiation equality. The difference between the mass scales arises because PBHs form from radiation, while halos form from matter.

Figures 6.2 and 6.3 show also the distribution of the collapsed region before halo formation. As it was discussed before the collapsed region forms a halo only after it becomes locally matter dominated, which occurs at $a \sim e^2 a_{eq}$, where e is the ellipticity of the region's initial tidal field. Typically, ellipticity varies from 0.1 to 0.3, local matter domination occurs around $a \sim 10^{-5}$ within regions that have collapsed by then, so most of the halos have the formation time $a_f \sim 10^{-5}$.

6.6 Conclusion

All in all, to discuss the abundance of the ultradense dark matter halos, this chapter covered the Press-Schechter formalism and its extension, Excursion Set formalism. The power spectrum resulting out of the latter formalism is (6.5). The Excursion Set formalism takes into account non-radial evolution of the overdense region, unlike the Press-Schechter one. Figure 6.2 shows the differential dark matter mass fraction for this power spectrum.

Primordial black holes and dark matter halos arise from the same power spectrum [18]. The differential dark matter mass fraction resulting from (6.16) is depicted in the Figure 6.3 [15].

Chapter 7

Gravitational Lensing Constraints

7.1 Introduction

Gravitational lensing is a phenomenon in astrophysics and cosmology where the gravitational field of a massive object, such as a galaxy or a galaxy cluster, bends and distorts the path of light from a more distant background object. This effect is a consequence of Einstein's theory of general relativity and has several important implications and applications in the study of the Universe. According to general relativity, massive objects warp the spacetime around them. When light from a distant object, like a quasar or a galaxy, passes near a massive foreground object, the path of the light is bent due to this curved spacetime. This bending causes the distant object's light to follow a curved trajectory as it passes the massive foreground object. There are several types of gravitational lensing: strong lensing, weak lensing and microlensing. This chapter focuses on the microlensing. Microlensing occurs when a compact object, like a star or a planet, passes in front of a background star. It causes a temporary increase in brightness of the background star, which can be observed when the foreground object is a massive compact halo object (MACHO). One of the potential applications of microlensing is the search for dark matter in the form of MACHOs. MACHOs are hypothetical dark matter candidates that could be composed of objects like brown dwarfs, black holes, or other compact, non-luminous objects. If ultra-dense dark matter halos consist of MACHOs or other compact objects, they could cause gravitational microlensing events when they pass in front of background stars. These microlensing events can be observed, and their statistical properties can be used to constrain the properties of the dark matter objects. By studying the rate and characteristics of microlensing events, astronomers can place limits on the abundance and mass distribution of MACHOs or other compact dark matter candidates in the Milky Way's halo, where dark matter is thought to be abundant.

This Chapter focuses particularly on constraining ultradense dark matter halos with the help of gravitational microlensing. Sections 7.2, 7.3 introduce a framework for this purpose. Section 7.4 provides the results from constraints using different surveys on ultradense dark matter halos resulting from different power spectrum as well as discussion on the constraints on PBHs. Section 7.5 provides calculations on how to connect the primordial power spectrum amplitude with the density fraction and therefore derive a constraint.

7.2 Gravitational Microlensing

Gravitational lensing is the transient, achromatic magnification of a star due to a transiting object, which offers opportunities to discover dark matter in macroscopic structures

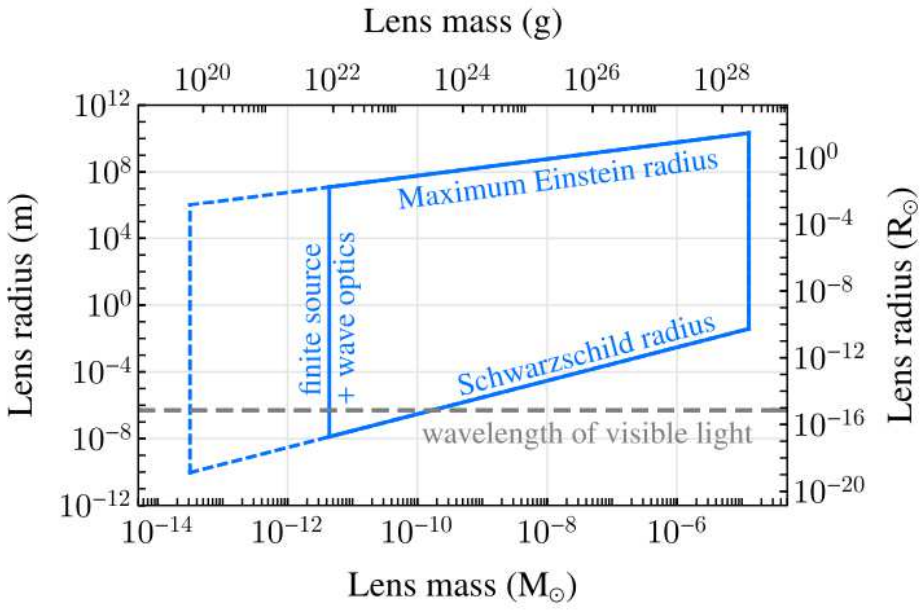

Figure 7.1: Sensitivity of the survey to generic dark matter structures in the space of lens size and mass[13].

weighing between asteroid and solar masses. The populations of effectively pointlike lenses, primordial black holes and MACHOs, have been constrained across a wide range of dark matter masses by surveys such as EROS/MACHO [3], OGLE [31], and Subaru-HSC [32]. The microlensing signal is appreciable when the lens comes within the Einstein radius along the line of sight between observer and source star.

We denote the lens mass by M, and the observer-lens, observer-source, and lens-source bu D_L, D_S and $D_{LS} = D_S - D_L$, respectively. The Einstein radius of a pointlike lens is given by, [13]

$$R_E = \sqrt{\frac{4GM}{c^2}\frac{D_L D_{LS}}{D_S}} = \sqrt{\frac{4GMD_S}{c^2}x(1-x)} \tag{7.1}$$

with $x \equiv D_L/D_S$. The Einstein radius, R_E is the closest approach to the lens of light rays from the source to the observer when the lend lies along the line of sight. It is also a useful distance scale with respect to which we normalize other distances.

Complication arises when the angular extent of source stars corresponds to a distance at the lens larger than the Einstein radius. This suppresses the magnification relative to pointlike sources. The effect is applicable particularly to the Subaru-HSC survey of M31 because of its sensitivity to small transit times and hence small Einstein radii.

In paper [13], they consider microlensing constraints on extended dark matter structures using Subru-HSC survey. Figure 7.1 shows the approximate sensitivity of the survey to generic dark matter structures in the space of lens size and mass. The dashed line shows the sensitivity that could be achieved without the effects of the sources' finite size and without the effects of wave optics. The lowest and highest masses probed are determined respectively by the smallest and largest transit time scales to which the survey is sensitive. For lenses much larger than the maximum Einstein radius of the setup, the lens becomes too diffuse to magnify source stars appreciably. Besides, lens sized of a given mass are bounded from below by the Schwarzschild radius corresponding to that mass.

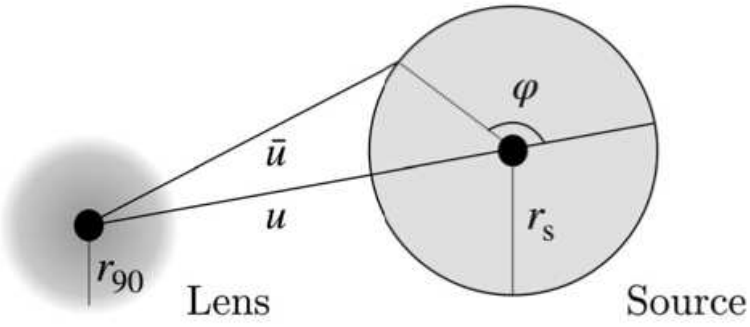

Figure 7.2: Geometry of the setup projected on the lens plane, [13].

7.3 Microlensing Constraints on Ultradense Dark Matter Halos

To determine th constraints on dark matter structures by the Subaru-HSC experiment, consider the microlensing signals from extended sources by extended lenses. Dark matter halos are intrinsically extended objects, therefore it is important to take into account for their size when deriving their potential lensing signatures. The setup to obtain the magnification of images is depicted in Figure 7.2.

The relevant distance scales along the line of sight (D_S, D_L) are typically much larger than those in the transverse direction, e.g. R_E, in the microlensing surveys that are considered. This means that we can treat the lensing as occurring entirely in the transverse place containing the lens. Therefore it is useful to view the lensing setup projected onto this plane with all distances expressed in units of R_E as in Fig. 7.2. In units of R_E, the source radius in the lens plane is $r_s \equiv sR_*/R_E$, the distance from the lens center to the source center is u, and to an arbitrary point on the edge of the source is

$$\bar{u}(\phi) = \sqrt{u^2 + r_s^2 + 2ur_s \cos\phi} \tag{7.2}$$

The lensing equation describing the trajectory of light rays after passing the lens plane, for every infinitesimal point on the edge of the source

$$\bar{u}(\phi) = t(\phi) - \frac{m(t(\phi))}{t(\phi)} \tag{7.3}$$

Solving this yields the positions of infinitesimal images at $t_i(\bar{u}(\phi)) \equiv \theta_i/\theta_E$ with i labeling multiple solutions. It is convenient to introduce Einstein angle, θ_E

$$\theta_E \equiv \sqrt{\frac{4GM_0}{c^2}\frac{D_{LS}}{D_L D_S}} = \sqrt{\frac{4GM_0}{c^2}\frac{(1-x)}{xD_S}} \tag{7.4}$$

and the Einstein radius can be expressed as $R_E \equiv D_L\theta_E$.

The mass profile, $m(t)$, is the distributions of the lens mass projected onto the lens plane. For spherically symmetric density profile $\rho(r)$, [14]

$$m(t) = \frac{\int_0^t d\sigma\sigma \int_0^\infty d\lambda\rho(R_E\sqrt{\sigma^2+\lambda^2})}{\int_0^\infty d\gamma\gamma^2\rho(R_E\gamma)} \tag{7.5}$$

7.3.1 Detectability of a microlensing event

The light coming from a source is deflected by the gravitational field of an object (lens). For low-mass lenses, the deflection cannot be resolved, but only a modification of the flux F, defined as

$$\mu \equiv \frac{\mathcal{F}}{\mathcal{F}_0} \tag{7.6}$$

where $\mathcal{F}_0$ is the flux in the absence of lensing. It is convenient to define β as the true source position angle with respect to the axis passing though the lens center, θ as the angle of the observed lensed image of the source. Then the lensing equation can be expressed as

$$\beta = \theta - \frac{\theta_E^2}{\theta}\frac{M_0(\theta)}{M_0} \tag{7.7}$$

where $M_0(\theta) = M_{2D}(D_L\theta)$ is the lens mass projected onto the lens plane, defined as before Eq. (5.42).

The magnification produced by an image i is given by the ratio of the image area to the source area

$$\mu_i = \frac{1}{4\pi r_s^2}\left(2\eta\int_0^{2\pi} d\phi \frac{d\psi}{d\phi} t_i^2(\phi)\right) \tag{7.8}$$

where $\eta = sgn(dt_i^2/d\bar{u}^2)|_{\phi=\pi}$ while the angular measure is defined from the angle ψ as

$$\tan\psi \equiv \frac{r_s \sin\phi}{u + r_s\cos\phi} \tag{7.9}$$

The overall total magnification is defined as the sum of the individual contributions

$$\mu_{tot} = \sum_i \mu_i \tag{7.10}$$

In this treatment, the wave optics effects, that are relevant when computing the magnification from lenses whose size is smaller than the wavelength of the detected , can be ignored. For the masses considered, the finite source size effect dominates the suppression of lensing signatures below $M \sim 10^{-11} M_\odot$. Therefore, the wave effects can be neglected.

In the limit of negligible source size ($r_s \ll u$) and pointlke lens ($R_{90} \ll R_E$), with R_{90} defined as the radius at which 90 per cent of the total mass is contained, $R_{90} = 32 r_h$. The analytical solutions in these limits to the lens equation

$$\mu_{tot} = \frac{2+u^2}{u\sqrt{u^2+4}} \tag{7.11}$$

In the opposite limit of a very large source, $r_s \gg u$, the lensing solutions give a large suppression of μ. This is because the lens only affects a negligible fraction of light rays coming from the source.

The lensing surveys, such as EROS, OGLE, and Subaru-HSC define as detectable a microlensing event whose temporary magnification of the source star exceeds the threshold value $\mu_{th} = 1.34$. Following this criterion, we require $\mu_{tot} > \mu_{th}$. The impact parameter, $u_{1.34}$, can be depicted as a funciton of both the size of the source, r_s, and the size of the lens, r_{90} (Figure 7.3).

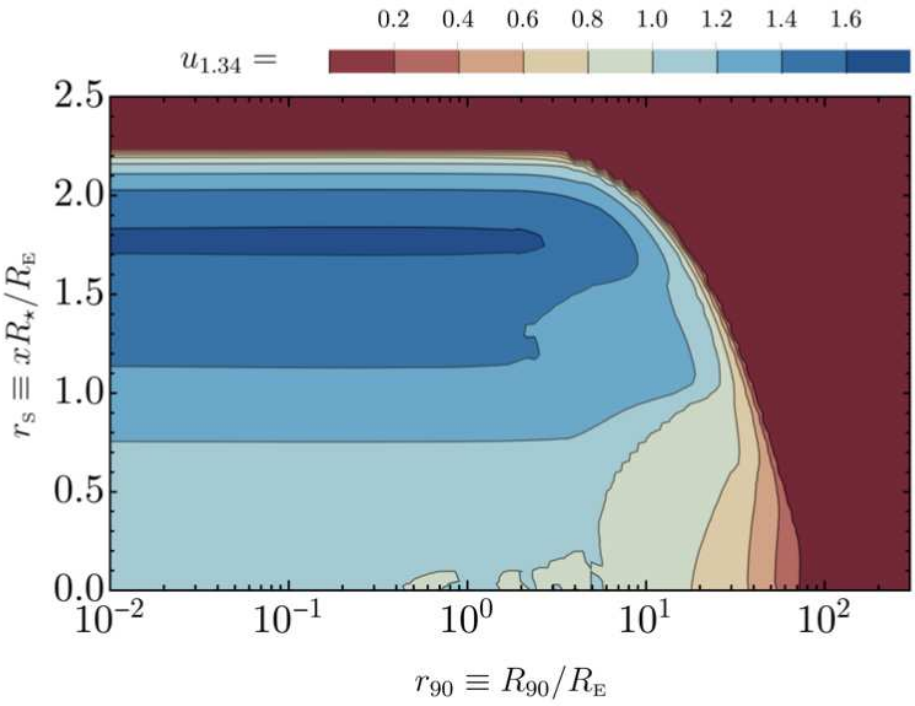

Figure 7.3: The threshold impact parameter as a function of the source size and the size of the lens [14].

7.3.2 Number of Detectable Events

The number of detectable lensing events can be computed by integrating the rate of overthreshold signals. For a single source star and unit exposure time, the differential events rate with respect to the halo mass distribution, $x = D_L/D_S$, and event timescale t_E, can be written as

$$\frac{d^2\Gamma}{dxdt_E d\ln M_0} = \left(\frac{d\rho_{lens}(x)}{d\log M_0}\right)\frac{2D_S\epsilon(t_E)Q^2(x)}{M_0 v_0^2}e^{-Q(x)/v_0^2} \tag{7.12}$$

where v_0 is the circular velocity in the galaxy. The differential density distribution of lenses $\rho_{lens}(x)$ can be derived as

$$\frac{d\rho_{lens}(x)}{d\log M_0} \equiv \frac{df_0}{d\log M_0} \times \rho_{DM}(x) \tag{7.13}$$

The function $Q(x)$ introduced earlier is

$$Q(x) \equiv 4\left(\frac{u_{1.34}(x)R_E(x)}{t_E}\right)^2 \tag{7.14}$$

and $\epsilon(t_E)$ is the efficiency of telescopic detection.

The total number of detectable events N_{events} is

$$\frac{N_{events}}{N_* T_{obs}} = \int d\log M_0 dR_* dt_E dx\left(\frac{d^2\Gamma}{dxdt_E d\log M_0}\frac{dn}{dR_*}\right) \tag{7.15}$$

where N_* is the number of observed source stars in the survey, T_{obs} is the total observation time and dn/dR_* is the distribution of source star radii.

7.4 Constraints on the power spectrum at small scales

Now let's test the sensitivity of microlensing to the ultradense halos arising from a broader family of primordial curvature power spectra. Consider realistic narrow spectra as a benchmark,

$$\mathcal{P}_\zeta^{\rm PL+Exp}(k) = A_0 \left(\frac{k}{k_0}\right)^4 \exp\left(2 - 2(k/k_0)^2\right) \tag{7.16}$$

which is parameterized by the peak amplitude A_0 and wave number k_0 such that the maximum is achieved at $\mathcal{P}_\zeta^{PL+Exp}(k_0) = A_0$. This spectrum grows as $\mathcal{P}_\zeta(k) \propto k^4$ for $k < k_0$, while it is Gaussian suppressed for $k > k_0$. The precise form of the small-scale suppression is not important for our constraint. It can be checked by considering the functional form

$$\mathcal{P}_\zeta^{\rm PL+PL}(k) = \frac{2A_0}{\left((k/k_0)^{-4} + (k/k_0)^4\right)^{-1}} \tag{7.17}$$

This spectrum similarly peaks at k_0, $\mathcal{P}_\zeta^{\rm PL+PL}(k_0) = A_0$ and grows as $\propto k^4$ for $k < k_0$, but for $k > k_0$ it decays as $\propto k^{-4}$.

The Press-Schechter mass functions from Eq. (num), when evaluated using the real-space top-hat window function, are not well behaved when the power spectrum decays rapidly at small scales. They predict a halo count that diverges at small mass scales, even when there is no power on such scales. This arises from the assumption of uncorrelated steps in the excursion set formulation of Press-Schechter theory, which corresponds to the use of a sharp k-space window function, $W(x) = \theta_H(c - x)$, instead of the top-hat window, with c, a constant, which fixes the connection between the wavenumber and the mass scale, θ_H, the Heaviside step function. Therefore we adopt the sharp k-space window when evaluating σ_M in (6.12).

The resulting halo distribution is depicted in Figure 7.4. The upper panel depicts the differential mass fraction in halos as a function of formation mass M. The middle panel shows the characteristic density of the halo, ρ_h, as a function of formation mass, M. And the lower panel shows the characteristic radius of the halo as a function of formation mass, M.

Note that even though the overall mass fraction f decreases with smaller peak amplitude, A_0, the corresponding halo density increases, Fig. 7.4. As the amplitudes of primordial perturbations decrease, the overdensities that can collapse to form ultradense halos are rarer and therefore increasingly spherical. This means that halos that form earlier in the history of the universe have larger internal density.

The parameter α, from the Eq.5.38, parametrizes theoretical uncertainty about the internal structures of ultradense halos. If we adopt a more moderate assumption, $\alpha = 30$, then the current constraint disappears and only future observations can constrain a smaller portion of parameter space. If we take the most conservative assumption, $\alpha = 1$, both current and future constraints disappear, as the lenses are then too diffuse to generate observable signatures within the Subaru-HSC survey.

The meaning of the values for the parameter α is as follows. Simulations during the matter dominated epoch suggest that the density of material within a halo is about 10^3 times the density of the universe at the time that the material became part of the halo. This consideration suggests $\alpha \simeq 10^3$, but the halo formation dynamics may be significantly different during the radiation epoch. So, the α parameter is free to vary. Generally, one expects that at least the matter density does not drop during the formation process, which suggests the lower limit for $\alpha \sim 1$.

The resulting constraints are depicted in the Figure 7.5, which shows the fraction of dark matter in terms of ultradense halos from a monochromatic halo mass distribution

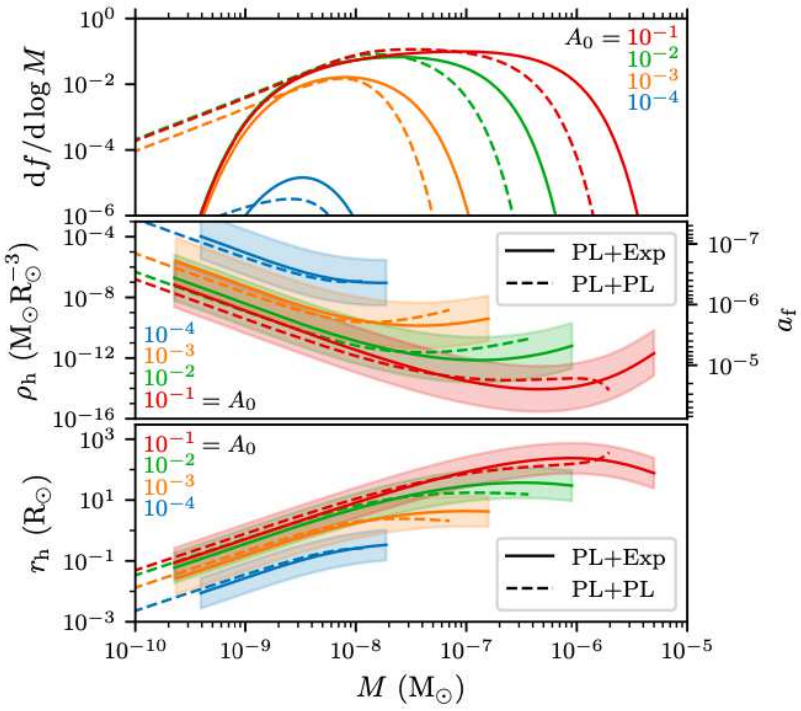

Figure 7.4: Ultradense halos arising from PL+Exp power spectrum and PL+PL power spectrum [14].

with respect to the halo mass, M_0. The constraints are shown by taking different values of the average density of the halos,

$$\bar{\rho} \equiv \frac{3M_0}{4\pi R_{90}^3} = \frac{\rho_h}{7300}. \tag{7.18}$$

From the Fig. 7.5, we can see that the density of the halo plays a crucial role for obtaining meaningful constraints from microlensing. For the lowest mass, the peak comes to $M_0 \simeq 10^{-9} M_\odot$, which is mostly constrained by the HSC survey. OGLE survey puts constraints dominantly at the masses around $M_0 \simeq 5 \times 10^{-5} M_\odot$. Lastly, EROS survey constraints mostly heavy masses around $M_0 \simeq 10^{-1} M_\odot$. More about the surveys can be read in Appendix A. If the limits for average density is taken to be $\bar{\rho} \lesssim 10^{-15} M_\odot / R_\odot^3$ for masses $M_0 < 10^{-2} M_\odot$ then the system doesn't have any constraints.

Besides, Figure 7.5 shows the final halo mass distribution, $df_0/d\log M_0$. Model A is taken from the Ref. [20] that considers the epoch of QCD phase transition, when the quarks were confined into hadrons. The distribution from this model crosses constraints from HSC and OGLE surveys for the average density to be at least $\bar{\rho} = 10^{-12} M_\odot / R_\odot^3$. However, taking into account the results from the Figure 6.1, it was realized that halos formed in this scenario are too large to be constrained by these surveys and setup.

7.4.1 Primordial Black Holes

To compare the lensing constraints with the PBH scenario, compute the power spectral amplitude required to generate PBHs with the power spectrum as in Equations 7.16, 7.17. First, consider the relationship between the cosmological horizon mass, M_H, and

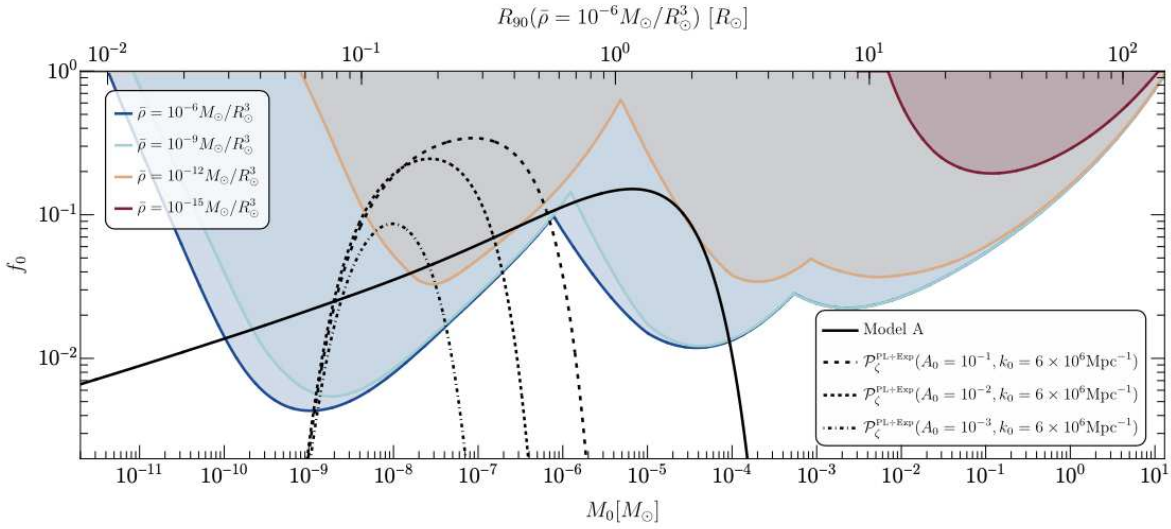

Figure 7.5: The fraction of dark matter in the form of ultradense halos with the assumption of monochromatic mass distribution. Colored lines show the mass fraction today with $f_0 = 3.5f$ and black curves illustrates the halo mass distribution, [14].

the comoving wave number, k,

$$M_H \simeq 17 M_\odot \left(\frac{g_*}{10.75}\right)^{-1/6} \left(\frac{k/\kappa}{\mathrm{pc}^{-1}}\right) \tag{7.19}$$

where g_* is the effective number of degrees of freedom, $\kappa \equiv k r_m$, with r_m being the characteristic perturbation size at horizon crossing. Next, compute the abundance of PBHs, f_{PBH}

$$f_{PBH} \equiv \frac{\Omega_{PBH}}{\Omega_{CDM}} = \frac{1}{\Omega_{CDM}} d\log M_H \left(\frac{M_{eq}}{M_H}\right)^{1/2} \beta(M_H) \tag{7.20}$$

where $M_{eq} \simeq 3 \times 10^{17} M_\odot$ is the horizon mass at matter-radiation equality, Ω_{CDM} is the dark matter density today. Using threshold statistics and computing the mass fraction assuming Gaussian primordial curvature perturbations, [14]

$$\beta(M_H) = \mathcal{K} \int_{\delta_l^{min}}^{\delta_l^{max}} d\delta_l \left(\delta_l - \frac{1}{4\Phi}\delta_l^2 - \delta_c\right)^\gamma P_G(\delta_l) \tag{7.21}$$

$$P_G(\delta_l) = \frac{1}{\sqrt{2\pi}\sigma(r_m)} e^{-\delta_l^2/2\sigma^2(r_m)} \tag{7.22}$$

where δ_l is the linear component of the density contrast and the integration boundaries are dictated by having overthreshold perturbations and type-I PBH collapse. $\sigma(r_m)$ is the variance of the linear density field computed at horizon crossing time and smoothed on a scale r_m. $\mathcal{K}$ and γ are introduced to include the effect of critical collapse, Φ controls the relationship between the density contrast and the curvature perturbations. Using the technique from [28] to compute the overdensity threshold, δ_c for PBH formation, the spectrum from (7.16) gives rise to collapsing peaks for which the characteristic comoving size is $\kappa \equiv k r_m = 2.51$ and the shape parameter is $\alpha_c = 4.14$, the threshold for collapse, $\delta_c = 0.572$, [14].

7.5 Constraints on the Primordial Power Spectrum Amplitude

In order to constrain the primordial power spectrum, we use the bounds on the equivalence fraction, f_{eq}. It can be assumed that f_{eq} is equal to the fraction of dark matter contained in the regions with overdensities, larger than the threshold to form ultradense minihalos, δ_{min}, but smaller than the threshold to form primordial black holes, $\sim 1/4$, then, [10]

$$f_{eq}(M_i) = \frac{2}{\sqrt{2\pi\sigma^2_{hor}(R)}} \int_{\delta_{min}}^{1/4} \exp\left(- \frac{\delta^2}{2\sigma^2_{hor}(R)} \right) d\delta \tag{7.23}$$

where R is the comoving radius containing a dark matter mass, M_i.

If we assume a scale dependence for the amplitude of the primordial power spectrum, $P_{\mathcal{R}(k)}$, we can then calculate using σ^2_{hor}. General approach for varius models of $P_{\mathcal{R}(k)}$ can be found in [8]. Whereas, in our case Ref. [27] summarizes similar approach.

In the matter dominated epoch (MD), the collapse overdensity is $\delta_c \simeq 1.686$. The amplitude of subhorizon density perturbation at MD epoch can be expressed as

$$\delta_\chi(k,z) = \frac{2}{5} \frac{k^2}{H_0^2 \Omega_M} T(k) \mathcal{D}(z) \mathcal{R}(k) \tag{7.24}$$

where $Omega_M$ is the matter density parameter today, $T(k)$ is the transfer function, $\mathcal{R}(k)$ is the curvature perturbations at horizon entry, and $\mathcal{D}(z)$ is the growth function, expressed as

$$\mathcal{D}(z) = \frac{(1+z)^2}{(1+z_{eq})^3} \left(2 + \left(\frac{1+z_{eq}}{1+z} - 2 \right) \sqrt{1 + \frac{1+z_{eq}}{1+z}} \right) \tag{7.25}$$

The curvature perturbation at some collapse redshift, z_c is required to be $\delta_\chi(k, z_c) = \delta_c$, with $z_c = 1000$, [8].

The dark matter overdensity is evaluated at the rest frame of the radiation and it is given by

$$\delta_\chi(k,a) = 6\mathcal{R}(k) \big(\ln\theta + \gamma_E - \frac{1}{2} - \mathrm{Ci}(\theta) + \frac{\sin theta}{2\theta} \big) \tag{7.26}$$

where γ_E is the Euler-Mascheroni constant, Ci is the cosine integral function, $\theta = \frac{k}{\sqrt{3}aH}$. At the horizon entry, $k = aH$, (7.26) becomes

$$\delta_{min}(k, z_c) = \frac{5}{6} \delta_c \frac{H_0^2 \Omega_M}{k^2 T(k)} \frac{0.988}{D(z_c)} \tag{7.27}$$

with $k = 5.1 \times 10^4 \mathrm{Mpc}^{-1}$, for which the mass $M_i = 10^{-3} M_\odot$ and $\delta_{min} = 2.2 \times 10^{-3}$.

Now, the relation between power spectrum and $\sigma^2(R,t)$

$$\sigma^2(R,t) = \int_0^\infty F^2(kR) \mathcal{P}_\chi(k,t) \frac{dk}{k} = \frac{1}{9} \int_0^\infty F^2(kR) \frac{k^4}{a^4 H^4} T_\chi^2(\theta) \mathcal{P}_\mathcal{R}(k) \frac{dk}{k} \tag{7.28}$$

where $F(x) = 3x^{-3}(\sin x - x\cos x)$ is the Fourier transform of the top-hat function, the transfer function, $T_\chi(\theta) \equiv \frac{\delta_\chi}{\theta^2 \mathcal{R}}$. Perform change of variables, $x \equiv kR$ and evaluate (7.28) at the horizon crossing

$$\sigma^2_{hor}(R) = \frac{1}{9} \int_0^\infty x^3 T_\chi^2 \left(\frac{x}{\sqrt{3}} \right) F^2(x) \mathcal{P}_\mathcal{R} \left(\frac{x}{R} \right) dx \tag{7.29}$$

If we assume that $\mathcal{P}_R$ is nearly constant, it can be pulled out of the integral and (7.29) becomes $\sigma^2_{hor}(R) \simeq 0.908 \mathcal{P}_R(k = R^{-1})$. And σ^2_{hor} yields the values of f_{eq}.

7.6 Conclusion

To conclude, the main goal of this chapter was to use the microlensing features to constrain ultradense dark matter halos. The key findings are illustrated in Figure 7.5, which shows the mass fraction and the halo mass distribution. One conclusion to draw from there is that the density plays a crucial role in obtaining meaningful constraints, so choosing proper range of the average density is important. For $\bar{\rho} \lesssim 10^{-15} M_\odot / R_\odot^3$ for the masses $M_0 < 10^{-2} M_\odot$, then the system will not have any constraints [14].

The microlensing features can be also used to put constrain the primordial black holes (PBH). It was found out that the threshold for the collapse leading to the formation of the PBH is $\delta_c = 0.572$ [14].

In order to improve the ability to constrain the data, there is a gap of knowledge that has to be addressed, namely, the internal density profile of the dark matter halo. This topic is a open question and it required more simulations of ultradense dark matter halos formation in the radiation epoch.

Chapter 8

Conclusion

Ultradense dark matter halos are prominent probes in the cosmology of the early Universe. The imprints in the power spectrum of energy density perturbations contain potential answers to the questions of the mechanism of inflation, the origin of dark matter and shine light to the opaque period of the Universe. Though the probes are prominent, there are uncertainties and challenges requiring further investigation. In this thesis work, the investigation of this topic from the cosmological perturbations that give rise to the cosmic structure, including dark matter halos. In Chapter 2, we derived the primordial power spectrum (2.7) and the evolution of the dark matter overdensity in the radiation dominated epoch (2.33). This allows to proceed further to study the collapse and the formation of the so-called dark matter protohalo in Chapter 3. The reason to call it a protohalo is due to the fact that the overdense region in the radiation dominated epoch after collapse doesn't form a halo until it becomes locally matter dominated [4]. We considered a spherical collapse from isothermal and adiabatic perturbations, the equations to describe these perturbations were derived fully (3.55, 3.61). A more realistic case would be the one, which takes into account non-radial evolution, namely, ellipsoidal collapse, described by (3.86). Chapter 4 provides calculations of the dynamics of the collapse of overdense region in the matter dominated epoch and further accretion process onto ultradense minihalo that formed in radiation epoch. Chapter 5 concludes with the properties of the ultradense dark matter halos, such as the core maximum size, density profiles and structures. Though the internal structure and density profile is yet unknown and is an open question. The factors that affect the formation of the internal structure of the ultradense dark matter halo are the nature of dark matter particle, annihilation of dark matter and inflow dynamics to the centre of the halo and the cosmological scenario [4]. To obtain a better understanding more simulations of ultradense dark matter halos formation should be done, for example [6]. Chapter 6 concludes on the abundance of the ultradense halos and primordial black holes. Lastly, Chapter 7 provides a way to constrain primordial power spectrum amplitude. However to obtain more conservative constraints more research in the internal structure of the ultrandese halos is required, namely more numerical simulations of the ultradense halos formation. Overall, the internal density of the ultrandense dark matter halos is an intriguing topic for further investigations. I hope to proceed further in my PhD research in this direction and learn more about computational tools such as GADGET, RAMSES, ENZO. These tools can help to design a simulation for the formation of the ultradense dark matter halo, having studied more of the key factors affecting this process.

Appendix A

Lensing Surveys

Lensing surveys refer to astronomical surveys that are designed to study gravitational lensing phenomena, particularly weak gravitational lensing, and their applications in astrophysics and cosmology. These surveys involve the observation and analysis of how the gravitational fields of massive objects, such as galaxies and galaxy clusters, distort and magnify the light from more distant background objects. Lensing surveys provide valuable insights into various aspects of the Universe, including dark matter distribution, the nature of dark energy, and the large-scale structure of the cosmos.

A.1 EROS

The EROS collaboration conducted gravitational microlensing surveys to search for dark matter objects and to study the distribution of matter in the Milky Way galaxy. The primary goal of EROS was to detect gravitational microlensing events caused by compact objects, such as dark matter particles, passing in front of background stars. Gravitational microlensing occurs when a massive object passes in front of a more distant background star. The gravitational field of the massive object acts as a lens, causing the light from the background star to be magnified and temporarily brightened. This phenomenon can provide insights into the distribution of dark matter in the Milky Way and the nature of dark matter particles. EROS surveys aimed to detect microlensing events caused by compact, massive objects that might be candidates for dark matter, such as MACHOs (Massive Compact Halo Objects) or other faint objects that do not emit significant light. In this appendix, the setup that was used in Ch. 7 is summarized here.

EROS-2 survey is focused on the observations of stars within the Large Magellanic Cloud (LMC), at a distance $D_S = 50$kpc away from Earth. The contribution of the Small Magellanic Cloud (SMC) was neglected in the analysis, since it is dim compared to the source of interest. The lenses of this setup are located in the Milky Way (MW). The density profile of the dark matter is isothermal one and is expressed as, [12]

$$\rho_{DM}(r) = \frac{\rho_s}{1 + (r/r_s)^2} \tag{A.1}$$

$$r \equiv \sqrt{R_{sol}^2 - 2xR_{sol}D_S \cos l \cos b + x^2 D_S^2} \tag{A.2}$$

with $\rho_s = 1.39\text{GeV/cm}^3$ the core density and $r_s = 4.38$kpc the core radius and $R_{sol} = 8.5$kpc the radial distance of the Sun, l and b are the longitude and the latitude of the source in galactic coordinates. In the case of LMC, $l = 238°$ and $b = -33°$. The number of observed stars, $N_* = 5.49 \times 10^6$, the observation time, $T_{obs} = 2500$ days. The efficiency factor, $\epsilon(t_E)$, of the EROS survey can be found in the Ref.[2]. EROS-2 LMC

survey observation revealed only one candidate for microlensing signature, $N_{obs} = 1$. The constraint obtained by the EROS survey is depicted in the Figure 7.5 for monochromatic mass distribution. The constraint is not effective anymore for values of the average density, $\bar{\rho} \gtrsim 10^{-9} M_\odot / R_\odot^3$. This is due to the fact that the lens of this size is smaller than the Einstein radius, R_E.

A.2 OGLE

OGLE-IV survey observes stars from the Milky Way (MW) galaxy. The density profile of the MW halo is taken to be isothermal one. The distance to the source stars is $D_S \simeq 8.5$kpc, the longitude and the latitude of the source in Galactic coordinates are $(l, b) = (1.09°, -2.39°)$. The number of the source stars that were used in the survey is $N_* = 4.88 \times 10^7$ and the observation time is $T_{obs} = 1826$ days. The number of candidate microlensing events over the observation time is 2622. The survey resulted in $N_{obs} = 6$ for $t_E \sim 0.1$ days, this can possibly constitute to PBH detection. To derive the constraint on the fraction of dark matter, f, this expression is used [11]

$$\kappa = 2 \sum_{i=1}^{N_{bins}} \left(N_i^{FG} - N_i^{SIG} + N_i^{SIG} \ln \frac{N_i^{SIG}}{N_i^{FG}} \right) \tag{A.3}$$

and it is required that $\kappa < 4.61$, which corresponds to the 90 per cent confidence level in Poisson statistics. Index i indicates the binning events by t_E , N_i^{DM} is the number of lensing signals induced by dark matter halos, N_i^{FG} is the number of astrophysical foreground events and $N_i^{SIG} \equiv N_i^{FG} + N_i^{DM}$. The constraint from the OGLE survey ranges for masses from $10^{-6} M_\odot$ to $10^{-6} M_\odot$ and is effective for $\bar{\rho} \gtrsim 10^{-9}$.

A.3 Subaru-HSC

Subaru-HSC survey used the stars from the M31 galaxy with the distance $D_S \simeq 770$ kpc from us. Lensing signatures in this survey arises both by M31 and MW compact structures. The circular speed for the MW galaxy is $v_0 = 220$ km/s and for the M31 is $v_0 = 250$ km/s. The differential event rate is the sum of each differential rate, $d\Gamma = d\Gamma_{MW} + d\Gamma_{M31}$. The density profile of dark matter is assumed to be NFW with scale density 0.184 GeV/cm^3 and the latitude and the longitude are $(l, b) = (121.2°, -21.6°)$. The number of stars in the HSC survey id $N_* = 8.7 \times 10^7$, the observation time is $T_{obs} = 7h$. The HSC survey constraints the lens masses much smaller than the previous surveys, EROS and OGLE.

Bibliography

[1] In: 471.2 (Nov. 1996), pp. 542–570. DOI: 10.1086/177989. URL: https://doi.org/10.1086%2F177989.

[2] In: 469.2 (Apr. 2007), pp. 387–404. DOI: 10.1051/0004-6361:20066017. URL: https://doi.org/10.1051%2F0004-6361%3A20066017.

[3] Ch Alcock et al. "EROS and MACHO combined limits on planetary-mass dark matter in the galactic halo". In: *The Astrophysical Journal* 499.1 (1998), p. L9.

[4] VS Berezinsky, VI Dokuchaev, and Yu N Eroshenko. "Formation and internal structure of superdense dark matter clumps and ultracompact minihaloes". In: *Journal of Cosmology and Astroparticle Physics* 2013.11 (2013), p. 059.

[5] Carlos Blanco et al. "Annihilation signatures of hidden sector dark matter within early-forming microhalos". In: *Phys. Rev. D* 100 (10 Nov. 2019), p. 103010. DOI: 10.1103/PhysRevD.100.103010. URL: https://link.aps.org/doi/10.1103/PhysRevD.100.103010.

[6] Carlos Blanco et al. "Annihilation signatures of hidden sector dark matter within early-forming microhalos". In: *Physical Review D* 100.10 (2019), p. 103010.

[7] JR Bond et al. "Excursion set mass functions for hierarchical Gaussian fluctuations". In: *Astrophysical Journal, Part 1 (ISSN 0004-637X), vol. 379, Oct. 1, 1991, p. 440-460. Research supported by NSERC, NASA, and University of California.* 379 (1991), pp. 440–460.

[8] Torsten Bringmann, Pat Scott, and Yashar Akrami. "Improved constraints on the primordial power spectrum at small scales from ultracompact minihalos". In: *Phys. Rev. D* 85 (12 June 2012), p. 125027. DOI: 10.1103/PhysRevD.85.125027. URL: https://link.aps.org/doi/10.1103/PhysRevD.85.125027.

[9] Bernard Carr et al. "Cosmic conundra explained by thermal history and primordial black holes". In: *Physics of the Dark Universe* 31 (2021), p. 100755. ISSN: 2212-6864. DOI: https://doi.org/10.1016/j.dark.2020.100755. URL: https://www.sciencedirect.com/science/article/pii/S2212686420304684.

[10] Bernard J Carr. *The Primordial black hole mass spectrum*. 1975.

[11] Djuna Croon, David McKeen, and Nirmal Raj. In: 101.8 (Apr. 2020). DOI: 10.1103/physrevd.101.083013. URL: https://doi.org/10.1103%2Fphysrevd.101.083013.

[12] Djuna Croon, David McKeen, and Nirmal Raj. "Gravitational microlensing by dark matter in extended structures". In: *Physical Review D* 101.8 (2020), p. 083013.

[13] Djuna Croon et al. "Subaru-HSC through a different lens: Microlensing by extended dark matter structures". In: *Physical Review D* 102.8 (2020), p. 083021.

[14] M Sten Delos and Gabriele Franciolini. "Lensing constraints on ultradense dark matter halos". In: *Physical Review D* 107.8 (2023), p. 083505.

[15] M Sten Delos and Joseph Silk. "Ultradense dark matter haloes accompany primordial black holes". In: *Monthly Notices of the Royal Astronomical Society* 520.3 (2023), pp. 4370–4375.

[16] M Sten Delos and Simon D M White. "Inner cusps of the first dark matter haloes: formation and survival in a cosmological context". In: *Monthly Notices of the Royal Astronomical Society* 518.3 (Nov. 2022), pp. 3509–3532. DOI: 10.1093/mnras/stac3373. URL: https://doi.org/10.1093%2Fmnras%2Fstac3373.

[17] M. Sten Delos, Margie Bruff, and Adrienne L. Erickcek. "Predicting the density profiles of the first halos". In: *Physical Review D* 100.2 (July 2019). DOI: 10.1103/physrevd.100.023523. URL: https://doi.org/10.1103%2Fphysrevd.100.023523.

[18] VI Dokuchaev and Yu N Eroshenko. "A common origin of neutralino stars and supermassive black holes". In: *arXiv preprint astro-ph/0202021* (2002).

[19] AG Doroshkevich. "Spatial structure of perturbations and origin of galactic rotation in fluctuation theory". In: *Astrophysics* 6.4 (1970), pp. 320–330.

[20] Gabriele Franciolini et al. "From inflation to black hole mergers and back again: Gravitational-wave data-driven constraints on inflationary scenarios with a first-principle model of primordial black holes across the QCD epoch". In: *Physical Review D* 106.12 (2022), p. 123526.

[21] Dmitry S Gorbunov and Valery A Rubakov. *Introduction to the theory of the early universe: Cosmological perturbations and inflationary theory*. World Scientific, 2011.

[22] Edward R Harrison. "Fluctuations at the threshold of classical cosmology". In: *Physical review D* 1.10 (1970), p. 2726.

[23] Lars Hernquist. "An analytical model for spherical galaxies and bulges". In: *Astrophysical Journal, Part 1 (ISSN 0004-637X), vol. 356, June 20, 1990, p. 359-364.* 356 (1990), pp. 359–364.

[24] Keisuke Inomata et al. "Double inflation as a single origin of primordial black holes for all dark matter and LIGO observations". In: *Phys. Rev. D* 97 (4 Feb. 2018), p. 043514. DOI: 10.1103/PhysRevD.97.043514. URL: https://link.aps.org/doi/10.1103/PhysRevD.97.043514.

[25] Edward W. Kolb and Igor I. Tkachev. "Large amplitude isothermal fluctuations and high density dark matter clumps". In: *Phys. Rev. D* 50 (1994), pp. 769–773. DOI: 10.1103/PhysRevD.50.769. arXiv: astro-ph/9403011.

[26] Eiichiro Komatsu et al. "Five-year wilkinson microwave anisotropy probe* observations: cosmological interpretation". In: *The Astrophysical Journal Supplement Series* 180.2 (2009), p. 330.

[27] Fangda Li, Adrienne L Erickcek, and Nicholas M Law. "A new probe of the small-scale primordial power spectrum: astrometric microlensing by ultracompact minihalos". In: *Physical Review D* 86.4 (2012), p. 043519.

[28] Ilia Musco et al. "Threshold for primordial black holes. II. A simple analytic prescription". In: *Phys. Rev. D* 103 (6 Mar. 2021), p. 063538. DOI: 10.1103/PhysRevD.103.063538. URL: https://link.aps.org/doi/10.1103/PhysRevD.103.063538.

[29] Julio F Navarro. "The structure of cold dark matter halos". In: *Symposium-international astronomical union*. Vol. 171. Cambridge University Press. 1996, pp. 255–258.

[30] Julio F Navarro, Carlos S Frenk, and Simon DM White. "A universal density profile from hierarchical clustering". In: *The Astrophysical Journal* 490.2 (1997), p. 493.

[31] Hiroko Niikura et al. “Constraints on Earth-mass primordial black holes from OGLE 5-year microlensing events”. In: *Physical Review D* 99.8 (2019), p. 083503.

[32] Hiroko Niikura et al. “Microlensing constraints on primordial black holes with Subaru/HSC Andromeda observations”. In: *Nature Astronomy* 3.6 (2019), pp. 524–534.

[33] Phillip James Edwin Peebles. *The large-scale structure of the universe*. Princeton university press, 2020.

[34] William H Press and Paul Schechter. “Formation of galaxies and clusters of galaxies by self-similar gravitational condensation”. In: *Astrophysical Journal, Vol. 187, pp. 425-438 (1974)* 187 (1974), pp. 425–438.

[35] Christoph Schmid, Dominik J Schwarz, and Peter Widerin. “Amplification of cosmological inhomogeneities by the QCD transition”. In: *Physical Review D* 59.4 (1999), p. 043517.

[36] Ravi K Sheth, HJ Mo, and Giuseppe Tormen. “Ellipsoidal collapse and an improved model for the number and spatial distribution of dark matter haloes”. In: *Monthly Notices of the Royal Astronomical Society* 323.1 (2001), pp. 1–12.

[37] Ya. B. Zeldovich. “A Hypothesis, unifying the structure and the entropy of the universe”. In: *Mon. Not. Roy. Astron. Soc.* 160 (1972), 1P–3P. DOI: 10.1093/mnras/160.1.1P.